Evolution of black holes in the centers of galaxies

Lucas Sommer

Munich 2012

Evolution of black holes in the centers of galaxies

Bachelor thesis

at the

Ludwig–Maximilians–Universitaet Munich

by

Lucas Sommer

(Matr. nr.: 100 88 116)

born in Alsfeld on 06/28/1989

supervised by

Prof. Dr. Andreas Burkert

and

Dr. Klaus Dolag

and

Rhea-Silvia Remus

Munich, August 10th, 2012

Evaluator: Prof. Dr. Andreas Burkert

Date for the oral examination:
  09/20/2012

Contents

Introduction

Observations of the inner area of nearby galaxies have provided evidence for the existence of super massive black holes (SMBHs) in the centers of galaxies. In combination with the existence of galaxies with active nuclei (AGNs), that are also assumed to contain super massive black holes, the investigation of black holes located in the central area of galaxies is of specific interest. Nevertheless, their real existence in the centers of galaxies is still only an assumption to explain observations, but not proven.

In order to accumulate evidence for the assumed existence of black holes in the centers of galaxies, this bachelor thesis primarily deals with comparisons of observational and simulated findings. These comparisons determine the validness of the simulated findings. In combination with this, the black holes typical evolution is investigated. While it manages to point out assumptions concerning the typical evolution of black holes in the simulation, it is also shown that the significance of these assumptions is challenged. In the discussed simulation, black holes are generated in the centers of galaxies with accretion rates larger than zero. As a result, a growth of mass and a radiation of energy by the black holes has to take place. The analysis is separated into two parts, the discussion of the accretion rate and the discussion of the luminosity function, and combined in the summary. Possible implications on the results of further observations in the end are given depending on the degree of validness of the description of observations by the simulation.

We present an abstract containing all physical principles used in the second chapter and the summary and conclusion in the first chapter. Here the basic principles of the expanding universe, black holes and AGNs are described. Fundamental physical constants and other measured variables, that are not explicitly given in the text, are listed in the appendix.

1 Theory

1.1 Basic principles of the expanding universe and black holes

In order to investigate the evolution of black holes in centers of galaxies this section should introduce some basic principles. These basics, on the one hand, concern the expansion of the universe in combination with redshift and cosmological time and, on the other hand, characteristics of black holes and possible ways of their appearance.

1.1.1 Expanding universe, redshift, cosmological time

For the discussion of the findings, it will be necessary to convert a given redshift into cosmological time. Therefore, it suggests itself to start with a short overview of the expansion equations of the universe and to show in this context, how to do the conversion of redshift into time.

Friedmann-equations. Starting with the cosmological principle, the assumption of homogeneity and isotropy of the universe, it is useful to define comoving coordinates to derive the expansion rate of the universe. The expansion rate leads to a generalization of Hubble's law. Comoving coordinates may be seen as spherical coordinates with its point of origin located in the center of a sphere with homogeneous density. In this case the sphere represents a part of the universe with the ability to expand radially and, as a result, a time-dependent but still homogeneous density $\rho(t)$. Starting with a point in time t_0 and an arbitrary position $\vec{r}(t_0) = \vec{x}$ in the sphere, the expansion with time leads to a new position,

$$\vec{r}(t) = a(t)\vec{x}. \tag{1.1}$$

Here a(t) is defined to be the **cosmic scale factor**. The cosmic scale factor for t_0 is set to $a(t_0) = 1$. In order to come to the expansion rate, defined as follows:

$$H(t) := \frac{\dot{a}}{a}, \tag{1.2}$$

one can derive Equation 1.1 with respect to time:

$$\vec{v}(t) = \frac{d}{dt}\vec{r}(t) = \frac{da}{dt}\vec{x} = \frac{\dot{a}}{a}\vec{r} =: H(t)\vec{r}. \tag{1.3}$$

As mentioned above this is a generalization of Hubble's law: $v = H_0 D$. Here D is the distance from the earth to a light emitting illuminant and $H_0 = H(t_0)$. In this case, t_0 correspond to present day and $H_0 = h100 kms^{-1}Mpc^{-1}$. In this case h is used in order to parametrize inaccuracy in measuring H_0 and is set to be $h = 0.704$ (see Komatsu et al. (2011)). Hubble's law was derived from the redshift, that is observed for most galaxies, and is a result of their radial movement pointing away from the earth. The **redshift** is defined as follows:

$$(1+z) = \frac{\lambda'}{\lambda_0} \qquad \text{respectively} \qquad z = \frac{d\lambda}{\lambda_0} = \frac{\lambda' - \lambda_0}{\lambda_0} = \frac{dv}{c}, \tag{1.4}$$

where λ' is the observed wavelength of the light, emitted by a source, e.g. a galaxy, and λ_0 is the wavelength in the reference system of the emitter. The last identity in Equation 1.4 is only valid for small redshift, where v holds $v \approx zc$. The idea of an expanding universe results of Hubble's law, that leads us to an expansion rate greater than zero in present day.

For further considerations of the expansion of the universe, equations of motion were derived by Friedmann by using the general theory of relativity. They are called **Friedmann-equations** and can be written as follows:

$$\left(\frac{\dot{a}}{a}\right)^2 = \frac{8\pi G}{3}\rho - \frac{Kc^2}{a^2}, \tag{1.5}$$

$$\frac{\ddot{a}}{a} = -\frac{4\pi G}{3}\left(\rho + \frac{3P}{c^2}\right). \tag{1.6}$$

These two equations depend on the density ρ and the pressure P. The first one

additionally depends on a constant K, while the value of K determins the evolution of the expansion. Density ρ and pressure P can also be written as

$$\rho = \rho_m + \rho_r + \rho_v, \qquad P = P_m + P_r + P_v = P_r + P_v, \qquad (1.7)$$

where the three indices represent "matter", "radiation" and "vacuum" . The matter component ρ_m characterizes the mass-density of matter, while $\bar{v} \ll c$. The matter component of the pressure P_m can be set to zero because $\frac{P_m}{c^2} \ll \rho_m$ (see Equation 1.6). For the radiation component $\bar{v} \approx c$ and P_r and ρ_r are linked by $P_r = \frac{1}{3}\rho_r c^2$. The vacuum component holds $P_v = -\rho_v c^2$ with $\rho_v = \frac{\Lambda}{8\pi G}$. In this case, Λ is the **cosmological constant**, that is assumed to be greater than zero. Using $\rho_m(t) = \rho_{m,0}a^{-3}(t)$, $\rho_r(t) = \rho_{r,0}a^{-4}(t)$, $\rho_v(t) = \rho_v = constant$ and $\rho_{crit} := \frac{3H_0^2}{8\pi G}$ one can define

$$\Omega_m := \frac{\rho_{m,0}}{\rho_{crit}}, \qquad \Omega_r := \frac{\rho_{r,0}}{\rho_{crit}}, \qquad \Omega_\Lambda := \frac{\rho_v}{\rho_{crit}} = \frac{\Lambda}{3H_0^2}, \qquad (1.8)$$

with $\Omega_m = 0.268$, $\Omega_r = 0.044$ and $\Omega_\Lambda = 0.728$ (see Komatsu et al. (2011)). In combination with 1.8 Equation 1.5 can be written as:

$$H^2(t) = H_0^2 \left[a^{-4}(t)\Omega_r + a^{-3}(t)\Omega_m - a^{-2}(t)\frac{Kc^2}{H_0^2} + \Omega_\Lambda \right]. \qquad (1.9)$$

For $H(t_0) = H_0$ and $a(t_0) = 1$, K turns out to be $K = (\frac{H_0}{c})^2(\Omega_m + \Omega_r + \Omega_\Lambda - 1)$, which leads to

$$H^2(t) = \left(\frac{\dot{a}}{a}\right)^2 = H_0^2[a^{-4}(t)\Omega_r + a^{-3}(t)\Omega_m + a^{-2}(t)(1 - \Omega_m - \Omega_\Lambda) + \Omega_\Lambda]. \quad (1.10)$$

From equations 1.8 and 1.10 it becomes evident, that the characteristics of the universe's expansion depend on the cosmological constant.The cosmological constant is, as mentioned above, assumed to be greater than zero.

Cosmological time and redshift. Using $dt = da(\frac{da}{dt})^{-1} = \frac{da}{aH}$, one comes to an expression for the cosmological time for a given cosmic scale factor by executing the integral:

$$t(a) = \frac{1}{H_0} \int_0^a [a^{-2}\Omega_r + a^{-1}\Omega_m + (1 - \Omega_m - \Omega_\Lambda) + a^2\Omega_\Lambda]^{-\frac{1}{2}} \, \mathrm{d}a$$

$$\approx \frac{1}{H_0} \int_0^a [a^{-1}\Omega_m + (1 - \Omega_m - \Omega_\Lambda) + a^2\Omega_\Lambda]^{-\frac{1}{2}} \, \mathrm{d}a. \tag{1.11}$$

In order to replace the scale-length-dependence by a redshift-dependence, the definition of the redshift given by Equation 1.4 can be used. In combination with Equation 1.3 and Equation 1.4, $d\lambda/\lambda_0$ can be written as follows:

$$\frac{d\lambda}{\lambda_0} = \frac{dv}{c} = \frac{H(t)}{c} dr = H dt = \frac{da}{a}. \tag{1.12}$$

The integration of $\frac{d\lambda}{da} = \frac{\lambda_0}{a}$ leads to: $\lambda(a) = Ca = \lambda'a$ respectively $\frac{1}{a} = \frac{\lambda'}{\lambda(a)}$, with C a constant. This leads to:

$$1 + z = \frac{1}{a}. \tag{1.13}$$

The combination of equations 1.11 and 1.13 with the approximation $\Omega_m + \Omega_\Lambda \approx 1$ (Einstein-de Sitter model) leads to an expression for t(z), that easily can be integrated. For this approximation the cosmological time turns out to be:

$$t(z) = \frac{2}{3H_0(1 + z)^{\frac{3}{2}}}. \tag{1.14}$$

For further information see Schneider (2008) chapters one and four.

1.1.2 Black holes

Concerning black holes, Shapiro and Teukolsky wrote: *"A black hole is defined simply as a region of spacetime that cannot communicate with the external universe. The boundary of this region is called the surface of the black hole, or the event horizon."* (Shapiro and Teukolsky (1983)). In order to understand this definition, it is described in the following subsection, how these objects form and which characteristics they have.

Onset of black holes. Stellar black holes can be formed by the gravitational collaps of stars when the energy recovery by nuclear fusion has come to an end.

Generally speaking, a physical systems is in an equilibrium condition when a balance of forces is reached. In case of an active star equilibrium condition means, that the absolute value of the gravitational force has to be equal to the absolute value of the force pointing outwards in radial direction from the center of the star, i.e.:

$$\vec{F}_{gravitational} = -\vec{F}_{radial} = -(\vec{F}_{centrifugal} + \vec{F}_{thermal} + \vec{F}_{radiation}). \tag{1.15}$$

The bond energy per nucleon has a maximum for iron. As a result, after the production of iron the nuclear fusion has to break, because no more energy can be gained by it. This leads to a decreasing radial force. In this case, the gravitational force dominates. This in turn leads to a contraction of the star.

The further evolution is strongly correlated with the mass and the mass density. If the mass is higher than the **Chandrasekhar limit**, $M_{Ch} \approx 1.5 M_{\odot}$, the force following from the Pauli principle by compressing fermions cannot break the compression and the gravitational collaps arises. A white dwarf forms out of the star. As mentioned above the further processing is also correlated to the density and thus to the radius of the object. If the particular radius of the object fulfills the following conditions:

$$R \leq \begin{cases} 5 \times 10^8 \text{cm (white dwarf)} \\ 3 \times 10^5 \text{cm (neutron star)} \end{cases}, \tag{1.16}$$

the white dwarf transforms into a neutron star or into a black hole. Black holes belonging to this type are called stellar black holes. Otherwise, the evolution may come to rest at white dwarf or neutron star level. For a detailed derivation of the Chandrasekhar limit and the radius respectively the density limit see Shapiro and Teukolsky (1983).

Characteristics. With respect to the equations of relativity, black holes may only have **three elementary properties**: *mass, angular momentum and electrical charge.* As mentioned above, there exists a distance defining the boundary of the black hole. Within this distance not even light has the ability to escape from the gravitational field produced by the black hole. According to this, for vanishing

Table 1.1: Classification of BHs, depending on the mass.

	Stellar BHs	IMBH	SMBH
Mass/$M_\odot$	1.5 - 100	100 - 10^5	$> 10^5$

angular momentum and electrical charge the distance is defined as:

$$r_s := \frac{2GM_\bullet}{c^2} = 2.9 \times 10^5 \text{cm} \frac{M_\bullet}{M_\odot}, \tag{1.17}$$

called the **Schwarzschild radius**. Although this is only an approximation, there is no need to investigate the boundaries of black holes in a more detailed way. To get further information see Schneider (2008) chapter one and four and Mueller (2010).

1.1.3 Super massive black holes in centers of galaxies

In accordance to the mass, black holes are separated in three categories. The two categories besides the *stellar black holes* are the *intermediate-mass black holes (IMBHs)* and the *super massive black holes (SMBHs)*. That means explicitly: black holes with a mass from 1.5 $M_\odot$ up to $10^2 M_\odot$ are called stellar black holes, those with $10^2 M_\odot$ up to $10^5 M_\odot$ are called intermediate-mass black holes and those with a mass higher than $10^5 M_\odot$ are called super massive black holes (see Table 2.4). IMBHs and SMBHs may form from stellar black holes by accretion or merging events.

In this subsection it should be explained, which reasons lead to the assumption of the existence of SMBHs in the center of the milky way and in the centers of other galaxies. Furthermore, the correlations of the properties of the centric black holes with the properties of the host galaxies are discussed.

The center of the milky way. Due to observations, it was possible to identify the galactic center to be Sagittarius A* (Sgr A*), which is a compact radio source with a very low own velocity and which itself is a part of Sagittarius A (Sgr A). The observation of individual stars in this inner region demonstrates, that the stars move on Keplerian orbits, which leads to the assumption of a nearly non-radiating massive object in the collective focus of the ellipses. This object has to have a very low latitude. Using the Keplerian laws (see box on page 8) and the measured velocity of the stars, one can calculate the mass of the central object with the help

of Equation 1.19:

$$M_\bullet \approx 3 \times 10^6 M_\odot. \tag{1.18}$$

It is nearby to identify this object in the center of the milky way with a black hole respectively with a SMBH, because the measurements for this region cannot be explained by an accumulation of stars and, moreover, there is also no other appropriate explanation.

The Keplerian laws (in matter of the solar system, *see Demtroeder (2005), p. 67*):

- All planets move on ellipses, with the sun located in one of the two focuses.

- The space, swept out by the vector between the sun and a planet, is equal for equal time slices.

- For all planets the square of the time of circulation divided by the cube of the semi-major axis is constant.

$$\Rightarrow v = \sqrt{\frac{GM_\bullet}{r}} \tag{1.19}$$

SMBHs in other galaxies. Additionally to the black hole in the center of the milky way and the assumption of the existence of SMBHs in the center of galaxies with an active galactic nucleus (discussed in Section 1.2), there are some more reasons to suppose the existence of black holes in the centers of further galaxies.

A black hole in the center of a galaxy cannot be observed by the given angular resolution directly, because its boundary, defined as the Schwarzschild radius (see Subsection 1.1.2), is to small. Nevertheless, one can measure its influence on the kinematics of the surrounding stars and gas by taking into account galaxies beeing not too far away from the earth. This influence arises, when the Keplerian velocity, described by Equation 1.19, becomes greater than or equal to the velocity dispersion σ in this inner region of the galaxy in regard. That means for $v_{Kepler} \approx \sigma$ the minimal distance r_{min} from the center, within the observation should be made, can

be calculated to be:

$$r_{min} = \frac{GM}{\sigma^2}.$$ (1.20)

As mentioned above, the available angular resolution leads to restrictions. Nevertheless, it was possible to detect a kinematic behavior in several cases by using spectroscopic methods, that suggest the assumption of Keplerian orbits in the inner region of many galaxies. As a result, a SMBH in their centers is assumed.

Correlations between black hole mass and velocity dispersion. Observations have pointed out a correlation between global properties of host galaxies and their central black holes described by the following equation:

$$log\left(\frac{M_{BH}}{M_\odot}\right) = \alpha + \beta log\left(\frac{\sigma}{\sigma_0}\right).$$ (1.21)

Here $\sigma_0 = 200km/s$ and σ is the velocity dispersion of the host galaxy, which is not equal to the velocity dispersion in the inner region of a galaxy also described by σ and used above. The parameters α and β are given by: $\alpha = 8.13 \pm 0.06$ and $\beta = 4.02 \pm 0.32$ (see Tremaine et al. (2002)), while the determination of β is not completed. For more information concerning black holes in centers of galaxies see Tremaine et al. (2002), Mueller (2010) and Schneider (2008) chapter three.

1.2 Active galactic nuclei (AGNs)

1.2.1 Introduction

In Subsection 1.1.3 the assumed existence of active black holes in the centers of some galaxies was already mentioned. This section deals with this topic in a continuative way. The attribute 'active' in this cases is to be understood as marking those black holes to play a striking role in the emission of electro-magnetic radiation by the totality of the galaxies' emission, they respectively belong to. Their particular role in the emission is originated in the accretion of matter upon them. As a result, the area surrounding the central black hole in such a galaxy in combination with the BH is called **active galactic nucleus (AGN)**. Because of the fact, black holes

and therefore also AGNs are the objects of investigation in this thesis, not only the most important properties of AGNs will be discussed in this section, but also further information should be presented.

It was already mentioned, that the difference between galaxies with and without an AGN may be found in the emission of electro-magnetic radiation. That means explicitly, that, nevertheless there exist differences in the appearance of AGNs, in most cases the luminosity of AGN-galaxies is superior by a few orders of magnitude than the luminosity of galaxies with a luminosity restricted more or less on the stellar components. For bright AGNs the bolometric luminosity may be $L \approx 10^{47} \frac{erg}{s}$. In observations appears the radiant source to be point-shaped and in deed the enlargement d of the inner region of the AGN seems to be restricted to less than $d = 2 \times 10^{-3} pc$ though radio waves are emitted by a region extending to more than one megaparsec and occurring as two lobes. Furthermore, the optical spectrum exhibits a continuous fraction extending from radio waves to x-rays or gamma rays and a fraction build up of wide emission lines. As it will be discussed below, but should already be mentioned here, these wide emission lines point to velocities higher than the typical velocities in galaxies without an AGN. Because of the enormous luminosity, observations of active galaxies are possible across long distances. This may lead to high redshifts as a result of the expansion of space.

A SMBH in the center. Once again, the origin of the assumption of the existence of SMBHs in the centers of galaxies has be motivated. This time for active galaxies. The most important reason leading to this assumption is the enormous amount of energy generation, that is needed for such a high luminosity emitted by a radiant source within a radial extension of one light day. As a result, the energy generation cannot be explained by nuclear fusion, as working in stars, but by the transformation of potential energy in attendance of the gravitational field of a SMBH. That process is called accretion and will be discussed in a separated subsection below (see Subsection1.2.3). Another aspect is the assumed existence of SMBHs in the centers of other galaxies. Although this argument was vice versa used for the explanation in Subsection 1.1.3, the argumentation is not circular, because it suggests itself to use a consistent theory for the description of as many galaxies as possible. This analogy between *'normal'* and *'active'* galaxies is the most important reason for the detailed discussion of SMBHs in the centers of galaxies, made above. It was already mentioned, that the radio wave-emitting regions extend

to megaparsec scales and occur as lobes. These lobes are expanded in a constant direction for long time scales. This might be explained by a rotating black hole with a constant direction of angular momentum.

Components of AGNs. Besides the already mentioned centrical black hole and the radio lobes arising as matter jets some more components within an AGN exist. In connection with the unification model, discussed in Subsection 1.2.2, the different components should be studied here. It is important to point out, that not all types of AGNs evidently have them in the same shape. The following list may give a short overview of their situation and their contribution to the electro-magnetic spectrum, whether their is one. The position of the particular components may be seen in Figure 1.1.
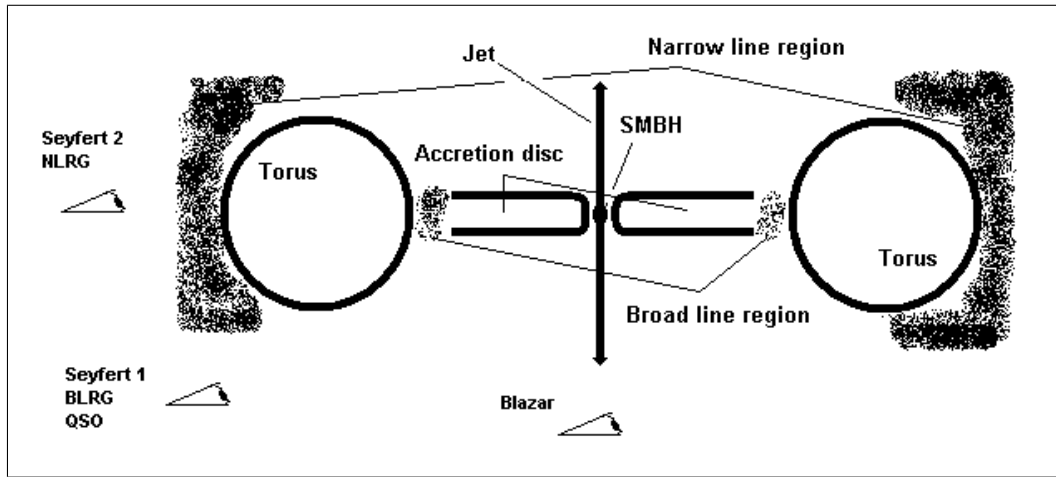
Figure 1.1: Components of an AGN

- **SMBH:** The black hole in the center provokes the gravitational potential, that is the driving existence in the AGN.

- **Accretion disc:** As a result of the angular momentum barrier, the gas streaming in cannot reach the black hole directly. This barrier results of the angular momentum of the individual gas particles. This becomes demonstrative when examining the energy for a two body problem. For $m_{gas} \ll M_{\bullet}$ we get

$$E = \frac{1}{2} m_{gas} \dot{r}^2 + \frac{L_{gas}}{2mr^2} + V_{grav}(r), \tag{1.22}$$

where m_{gas} is the mass of the gas particle, L_{gas} is its angular momentum, and V_{grav} is the gravitational potential, provoked by the black hole. The consideration of the limiting behavior of Equation 1.22 leads us to $\lim_{r \to 0} E = \infty$. As a result, the gas accumulates in a disk fulfilling Keplerian motion respectively differential motion, i.e. the angular velocity depends on the distance from the center. Because of the differential motion, friction forces occur in the disk and heat it up. This in turn leads to thermal emission of electro-magnetic waves. For a blackbody this radiation would follow Planck's law, but has to be modified for an accretion disk. Nevertheless, the thermal emission explains the existence of a continuous fraction in the spectrum.

- **Broad line region (BLR):** As mentioned above, a fraction containing emission lines exists besides the continuous spectrum. When taking into account the Doppler effect, the widest emission lines allow to suggest velocity of the emitting gas of about 10,000 km/s. In this region of the AGN, the emission of photons results from photoionization of gas by photons out of the continuous spectrum. This gas seems to be accumulated in clouds having a distance of $r \approx 1000 r_s$ from the center. This distance additionally depends on the luminosity of the AGN.

- **Narrow line region (NLR):** The emission lines occurring from this region allow to draw the conclusion, that the gas in this area moves with about 400 km/s. Here the same physical processes are in play as in the BLR. Observations of this region show a cone shaped distention possibly resulting of the dust torus. In the dust torus the photons of the continuous spectrum are scattered and are absent for photoinonization from this point in time.

- **Jets:** The extension of radiant sources emitting radio waves for over one megaparsec, was already mentioned above. These sources are build up of matter jets transporting electrons away from the black hole. As a result, electrons with relativistic velocities move in magnetic fields and emit synchrotron radiation, containing x-ray waves, optical waves, and radio waves.

Correlations between AGNs and their host galaxies. So far, only the active center of active galaxies was discussed. The existence of an AGN may also influence the properties of the whole galaxy or at least the temporal development may be correlated (see Fontanot et al. (2011)). These correlations e.g. refer to the mass of

the central SMBH and to the stellar mass, luminosity and velocity dispersion. I. e. galactic winds originating from the enormous luminosity of the AGN may remove a lot of cold gas and hence the star formation rate can be constrained. Moreover, merging events are thought to indicate active centers as well as leading to the build up of spheroidal shapes of galaxies. Within the scope of that, another correlation between the host galaxy and the AGN may be found.

1.2.2 Unification model for AGNs

In order to present the main features of the unification model, in this subsection several forms of appearance of AGNs occurring in observations are mentioned at first. From this listing it should become evident which components, presented in Subsections 1.2.1, each type of AGN is at least attached with, due to its contributions to the electro-magnetic emission.

- **Quasi-stellar objects (QSOs):** This type of galaxies containing an AGN is the most luminous one. Its electro-magnetic spectrum contains a continuous fraction, a fraction with broad and narrow emission lines, and a radio fraction. Different QSOs may differ in the intensity of their radio emission.

- **Seyfert galaxies:** These galaxies are distinguished into two types as a function of the intensity of their broad emission lines, while the luminosity is lower than that of QSOs. Observations demonstrate the host galaxies in this case to be spiral galaxies.

- **Radio galaxies:** The difference between Seyfert galaxies and this type is primarily the intensity of the radio emission. Due to its name, for radio galaxies it is higher than for Seyfert galaxies. Moreover, the host galaxies of this type are elliptical. In correlation with the Seyfert galaxies radio galaxies are distinguished into two types with respect to the intensity of their broad emission lines. I. e. narrow-line radio galaxies (NLRG) and broad-line radio galaxies (BLRG).

- **Blazars:** In this case, not only the intensity of the broad emission lines is a criterion for the distinction, but also the intensity of the narrow emission lines. The first type are the *optically violent variables (OVVs)*, whose spectra show emission lines, and the second type are *BL Lacs*, whose spectra do not show

emission lines at all. The presence of emission lines in the spectra seems to be related to the luminosity of the blazars, i. e. for highly luminous ones the emission of the jets dominates the spectrum. Furthermore, in both cases the luminosity varies in short time intervals, which may transform OVVs into BL Lacs and vice versa.

Unification. The unification of the AGNs leads to the model, shown in Figure 1.1. The difference in the form of appearance in this way is thought mostly to be a result of the viewing direction, while the shape of the components also leads to differences additionally to the differences in the shape of the host galaxies. The angle of sight-dependence may result of non-isotropic emission of the AGN, as it is shown in Figure 1.1. Another aspect leading to the different types, may be the angular momentum of the SMBH, its mass and the amount of matter available in the accretion disk.

1.2.3 Accretion, luminosity and Eddington limit

This subsection deals with the already mentioned accretion of matter onto a black hole in more details. Delivered in this, the temperature profile of the accretion disk, the limitations constraining the accretion itself (Eddington limit) and the period in time for markedly growth of the black hole by accretion are given.

Accretion and luminosity. The accretion disk originates from the accumulation of gas, initiated by the SMBH. The physical process in play in this case is the gravitation. The loss of gravitational energy in this central force field can be converted into kinetic energy. Following from the virial theorem (see box on page 16), only half of the potential energy is transformed into kinetic energy. The rest is transformed into intrinsic energy, i. e. in thermal energy resulting from friction. Once again it should be mentioned, that the friction occurs because of the differential rotation of the accretion disk (see Subsection 1.2.1). The energy, gained by a process transforming matter into energy according to the theory of special relativity, can be given by:

$$E = \epsilon m c^2, \tag{1.23}$$

where ϵ gives the efficiency of the transformation. For accretion ϵ may be about

0.06 for non-rotating and up to 0.29 for rotating black holes. Referring to the loss of potential energy the amount of thermal energy, gained by accretion, is:

$$\Delta E \approx \frac{1}{2} \frac{GM_\bullet m}{r^2} \Delta r, \tag{1.24}$$

where the factor $\frac{1}{2}$ appears because of the virial theorem (see Equation 1.26), and m stands for the mass of a body moving towards the center. The power in this case is in accordance with the luminosity, that is given as (see also box on page 16):

$$\Delta L = \Delta \dot{E} = \frac{1}{2} \frac{GM_\bullet \dot{m}}{r^2} \Delta r \qquad \text{respectively} \qquad \Delta L = 4\pi \Delta r \sigma_{SB} T^4(r), \tag{1.25}$$

where σ_{SB} stands for the Stefan-Boltzmann constant. The second Equation in 1.25 corresponds to the Stefan-Boltzmann law with its characteristic T^4-dependence, that is valid for a blackbody, multiplied with two according to the two sides of the accretion disk. The fact, that the Planck spectrum has to be modified for the accretion disk, was already mentioned. This is a result of the radius-dependence of the temperature of the disk. The temperature may be derived from Equation 1.25 to be: $T(r) = (\frac{3c^6}{64\pi\sigma_{SB}G^2})^{\frac{1}{4}}(\dot{m})^{\frac{1}{4}}(M_\bullet)^{-\frac{1}{2}}(\frac{r}{r_s})^{-\frac{3}{4}}$. In particular that means, that the disk cannot be seen as a blackbody with constant temperature. This in turn leads to the continuous spectrum.

Eddington limit. As comparable to stars, an equilibrium state may occur, when an equilibrium of forces is reached. In this case only the forces originated in radiation and gravitation are of interest. Accretion onto the black hole is only possible for:

$$\vec{F}_{gravitational} > -\vec{F}_{radiation} \qquad \text{respectively} \qquad \left|\vec{F}_{gravitational}\right| > \left|\vec{F}_{radiation}\right|, \tag{1.30}$$

where an isotropic emission of radiation was supposed. In order to come to an equation for $F_{radiation}$, only the scattering process at free electrons of the plasma has to be considered. Protons and nuclei can be neglected, because their scattering cross section is much smaller. This may be seen by taking into account the equation for the scattering cross section for the Thomson scattering, that is given by:

$$\sigma_T = \frac{8\pi}{3}\left(\frac{e^2}{4\pi\epsilon_0 mc^2}\right)^2, \tag{1.31}$$

The virial theorem (*see A. Weigert (2009), p. 12f*): This theorem is true for closed n particle systems being in an equilibrium state, while energy conservation is always given for closed systems. Furthermore, it is referred to the mean value for long time scales. It says:

$$E_{kin} = -\frac{1}{2}E_{pot} = -E_{ges} \qquad \text{respectively} \qquad \Delta E_{pot} = -2\Delta E_{kin}. \quad (1.26)$$

Luminosity (*see. A. Weigert (2009), p. 41f*): The luminosity gives the energy flux (energy per time) through a surface provided by a radiant source e. g. located in the middle of a sphere. In combination with the definition of the radiant flux, $F = \iint I sin(\Theta)\, d\Phi d\Theta$, the energy flux for a sphere with radius R is given by:

$$L = 4\pi R^2 F. \quad (1.27)$$

The radiation, yield by the radiant source, in the distance r from the source, than is given by:

$$S = \frac{L}{4\pi r^2}. \quad (1.28)$$

The distance r from the source for a given luminosity L and a given radiation S may also be defined as luminosity distance:

$$D_L(z) = \sqrt{\frac{L}{4\pi S}}. \quad (1.29)$$

It is important to note, that for the determination of the bolometric luminosity also the distance between the observer and the radiant source has to be known. Thus the magnitude is separated into apparent and absolute magnitudes, while the apparent magnitude may be observed and the absolute magnitude has to be calculated from the apparent. The attribute bolometric in this case refers to the summation of the luminosities respectively magnitudes for specific frequency intervals. The redshift-dependence of the luminosity distance in this case results of the expansion of space.

with $\sigma_T \propto \frac{1}{m^2}$. For Thomson scattering the force onto an electron is given by:

$$F_{radiation} = \frac{\sigma_T L}{4\pi r^2 c}.$$ (1.32)

From now on σ_T is the cross section for an electron calculated by Equation 1.31 with $m = M_e$ and r indicates the distance between the electron and the radiant source. Using equations 1.30 and 1.32 and Newton's law of gravitation, an upper limit for the luminosity can be derived to be:

$$L_{edd} := \frac{4\pi c G m_p}{\sigma_T} M_\bullet \approx 1.3 \times 10^{38} \frac{M_\bullet}{M_\odot} \frac{erg}{s} \qquad \textbf{(Eddington luminosity)}.$$ (1.33)

I. e. only for $L < L_{edd}$ accretion onto the SMBH is possible. Furthermore, it is possible to derive a lower limit for the mass of a SMBH in the center of an AGN for an observed luminosity:

$$M_\bullet > M_{edd} := \frac{\sigma_T}{4\pi c G m_P} L \approx 8 \times 10^7 \frac{L}{10^{46} \frac{erg}{s}} M_\odot.$$ (1.34)

Using Equation 1.23, the luminosity can also be written as:

$$L = \dot{E} = \epsilon \dot{m} c^2.$$ (1.35)

This leads to an equation for the accretion rate for a given ϵ and a given L,

$$\dot{m} = \frac{L}{\epsilon c^2} \approx 0.18 \frac{1}{\epsilon} \left(\frac{L}{10^{46} \frac{erg}{s}}\right) \left(\frac{M_\odot}{1yr}\right)$$ (1.36)

respectively

$$\dot{m} = \frac{L}{L_{edd}} \frac{1.3 \times 10^{38} \frac{erg}{s}}{\epsilon c^2} \frac{M_\bullet}{M_\odot} =: \frac{L}{L_{edd}} \dot{m}_{edd}.$$ (1.37)

In Equation 1.37 the Eddington accretion rate was defined, which indicates the maximal accretion rate onto a black hole.

Increase of mass in time. Due to accretion, the total mass of the SMBH has

to grow. When the accretion rate is constant in time, the equation

$$\dot{m} = \frac{\Delta M}{\Delta t} = \frac{M_{\bullet}}{t_{evolution}} \tag{1.38}$$

has to be valid. This leads to:

$$t_{evolution} = \epsilon(\frac{L}{L_{edd}})5 \times 10^8 yr. \tag{1.39}$$

Equation 1.38 will be used later on to investigate the evolution of black holes in AGNs.

1.2.4 Bolometric luminosity function of AGNs

Generally speaking, the luminosity function of AGNs for a fixed redshift z in words is defined to be the number of AGNs per volume with bolometric luminosities in a given interval [L,L+dL]. The definition may also be written as:

$$\Phi(L, z) := \frac{dN(L, z)}{dLdV(z)}, \tag{1.40}$$

where the redshift-dependence of the volume dV results from the expansion of space leading to comoving coordinates. This was discussed in Subsection 1.1.1. Because of the redshift-dependence of the luminosity function, its interpretation is very important for the understanding of the outcome and evolution of SMBHs as well as for the evolution of galaxies itself. This is due to the correlations between SMBHs and their host galaxies (see Subsection 1.1.3) and the correlations between AGNs and again their host galaxies (see Subsection 1.2.1).

Problems and results. The practical determination of the bolometric luminosity function is attached with a few problems. One difficulty is the restriction of observations on specific wavelength ranges in normal cases. Due to that, a generalization in order to come to the bolometric luminosity function is only valid, if the different spectral shapes for the wavelength ranges, the redshift of the detected photons, and darkening by interstellar medium (ISM) are taken into account. Moreover, the completeness of the measurement has to be given.

In order to come to a bolometric luminosity function, P. Hopkins, G. Richards and L. Hernquist took into account measurements of luminosity functions for QSOs

(Hopkins et al. (2007)). In contrast to the luminosity function of galaxies, that may be approximated by a Schechter function, they followed the common ansatz and used a double power law for fitting:

$$\Phi(L) = \frac{\Phi_*}{(\frac{L}{L_*})^{\gamma_1} + (\frac{L}{L_*})^{\gamma_2}} \tag{1.41}$$

respectively

$$\Phi(L) = \frac{\frac{\Phi'_*}{L_*}}{(\frac{L}{L_*})^{-\alpha} + (\frac{L}{L_*})^{\beta}} \qquad \textbf{(for optical wavelength range)}. \tag{1.42}$$

In this case, the redshift-dependence is associated with the parameters γ_1, γ_2, Φ_*, and L_* representing the best-fit parameters for the combination of the measurements and are given in Table 1.2. The other parameters in Equation 1.42 are given by $\alpha = -(\gamma_1 + 1)$, $\beta = -(\gamma_2 + 1)$, and $\Phi'_* = \frac{\Phi_*}{ln(10)}$.

Table 1.2: Best-fit parameters (see Hopkins et al. (2007)). ((1) Mpc^{-3}; (2) $L_\odot = 3.9 \times 13^{33} erg/s$)

$<z>$	$log(\Phi_\star{}^1)$	$log(L_\star)^2$	γ_1	γ_2
0.1	-5.45 ± 0.28	11.94 ± 0.21	0.868 ± 0.050	1.97 ± 0.17
0.5	-4.66 ± 0.26	12.24 ± 0.18	0.600 ± 0.136	2.26 ± 0.23
1.0	-4.63 ± 0.15	12.59 ± 0.11	0.412 ± 0.122	2.23 ± 0.15
1.5	-4.75 ± 0.19	12.89 ± 0.13	0.443 ± 0.145	2.29 ± 0.20
2.0	$.4.83 \pm 0.05$	13.10 ± 0.04	0.320 ± 0.046	2.39 ± 0.07
2.5	-4.96 ± 0.14	13.13 ± 0.09	0.302 ± 0.091	2.30 ± 0.15
3.0	-5.23 ± 0.12	13.17 ± 0.10	0.395 ± 0.060	2.10 ± 0.12
4.0	-4.66 ± 0.37	12.39 ± 0.32	-0.254 ± 0.736	1.69 ± 0.18
5.0	-5.38 ± 1.19	12.46 ± 1.10	0.497 ± 0.458	1.57 ± 0.41
6.0	-5.13 ± 0.38	11.0	0.0	1.11 ± 0.13

For more information concerning sections 1.2 see Schneider (2008) chapter fife, Mueller (2010), and Fontanot et al. (2011).

2 Simulation, findings and discussion

2.1 Simulation

In order to investigate the evolution of black holes we study a **cosmological, hydrodynamic simulation**. The code, P-GADGET3, used for the simulation is an extended version of GADGET2 (Springel et al. (2001)). It includes tree particle-mesh (TreePM) and smoothed particle hydrodynamics (SPH) methods. In P-GADGET3 cooling, star formation and supernova-driven winds (Springel and Hernquist (2003)), chemical enrichment from stellar population, AGB stars and SNe (Tornatore et al. (2004)), low-viscosity SPH (Dolag et al. (2005)), black hole growth and feedback from AGN (Springel et al. (2005), Fabjan et al. (2010)) are included.

The number of particles within the simulated, cubic box depends on the used resolution, while the edge length is $a = 48Mpc/h$. For *medium resolution (mr)* the box contains 2×81^3 particles, for *high resolution (hr)* 2×216^3 particles, and for *ultra high resolution (uhr)* 2×576^3 particles. As a result, the mass resolution for each resolution is also different. For *mr* $m_{dm} = 1.3 \times 10^{10} M_\odot/h$ and $m_{gas} = 2.6 \times 10^9 M_\odot/h$, for *hr* $m_{dm} = 6.9 \times 10^8 M_\odot/h$ and $m_{gas} = 1.4 \times 10^8 M_\odot/h$, and for *uhr* $m_{dm} = 3.6 \times 10^7 M_\odot/h$ and $m_{gas} = 7.3 \times 10^6 M_\odot/h$. According to WMAP7 (Komatsu et al. (2011)) the cosmological parameters Ω_m, Ω_r, Ω_Λ, and h are set to: $\Omega_m = 0.268$, $\Omega_r = 0.044$, $\Omega_\Lambda = 0.728$, and h = 0.704. The efficiency ϵ for the transformation of matter into energy, described by Equation 1.23, is 0.1. The indices of the snapshots correspond to redshifts. The redshifts are given in the discussion, when used.

2.2 Findings and discussion

2.2.1 Accretion rate

In the discussed simulation, all black holes are created in the centers of galaxies when the galaxy crosses a given mass limit. This limit depends on the chosen resolution and shifts to lower values with increasing resolution. As a result, most of the simulated black holes can be classified as SMBHs, or at least as IMBHs (see Table 2.4). Furthermore, the so called seeding of black holes starting with a given mass limit leads to the characteristic sharp dividing line for the lower limit of masses shown in figures 2.1, 2.2, and 2.3. The consideration of the accretion rate in the simulation is of specific interest, because it plays an important role in the evolution of the black holes. I. e., on the one hand, it determines the growth of mass, and, on the other hand, it enables the calculation of the bolometric luminosity. Therefore, the evolution of the accretion rate, especially its correlation with mass for the whole population of black holes, should be discussed in this subsection. The accretion rate in the studied simulations is implemented to be proportional to the density of surrounding gas and the square of the black holes mass. As a result of the proportionality to the square of the mass, problems concerning the description of the accretion rate for relatively low masses occur. This has to be taken into account especially in combination with the resolution dependence of the mass limit for the seeding of black holes. Furthermore, uncertainty about the reliability of the numerical methods used in the high resolution simulations are still left.

In order to investigate the evolution, at first a comparison of observational and simulated findings concerning black holes in the centers of galaxies in combination with a short description of the simulated data will be done. In a second step, the findings are discussed in more detail. The comparison of the simulated data with observational findings helps to classify possible predictions, made by the analysis of the simulation. Observational data for several types of AGNs are given in Table 2.5.

Description and comparison. The simulated findings depend on the chosen resolution, *mr*, *hr*, or *uhr*. Thus for each data set the values are presented separately, but compared with observational data in one.

- **Medium resolution:** Black holes are present for redshifts reaching from z = 3.3810 to z = 0.0, while the mass range of the black holes within this

redshift interval expands from $M_{\bullet,min} \approx 10^6 M_\odot$ to $M_{\bullet,max} \approx 10^{10} M_\odot$. Including all data for all redshifts we find, that the lowest accretion rate, $\dot{m}_{min} \approx 10^{-16} M_\odot/s$, occurs for a black hole having a mass of $M_\bullet \approx 3.5 \times 10^6 M_\odot$, and the highest accretion rate, $\dot{m}_{max} \approx 10^{-6} M_\odot/s$, occurs for a black hole having a mass of $M_\bullet \approx 3 \times 10^9 M_\odot$. All accretion rates are lower than the corresponding Eddington accretion. As shown in Figure 2.1, the typical values of the accretion rate are correlated with the mass range, the black holes are located in. This leads to three groups. I. e., for black holes having masses from $10^6 M_\odot$ up to $2 \times 10^7 M_\odot$ the accretion rate reaches from 0.1% up to approximately 100% of the Eddington accretion rate. For black holes having masses from $2 \times 10^7 M_\odot$ up to $3 \times 10^8 M_\odot$ the accretion rate reaches from 1% up to 100% of the Eddington accretion rate. And for black holes having masses from $3 \times 10^8 M_\odot$ up to $10^{10} M_\odot$ the accretion rate reaches from 0.1% up to 10% of the Eddington accretion rate (see also Table 2.1). The Eddington limit is plotted in Figure 2.1 as a continuous line, while each cross represents an individual black hole.

Table 2.1: Correlation of mass range and characteristic accretion rate (mr).

Group	I	II	III
$M_\bullet/M_\odot$	$10^6 \ - \ 2 \times 10^7$	$2 \times 10^7 \ - \ 3 \times 10^8$	$3 \times 10^8 \ - \ 10^{10}$
$\dot{m}/\dot{m}_{Edd}$	$0.001 \ - \ \approx 1$	$0.01 \ - \ 1$	$0.001 \ - \ 0.1$

- **High resolution:** As for the mr sample, the redshifts at which black holes are present reach from z = 3.3810 to z = 0.0. The lower mass limit shifts to $M_{\bullet,min} \approx 2 \times 10^5 M_\odot$, and the upper limit stays at $M_{\bullet,max} \approx 10^{10} M_\odot$. The interval of the accretion rates is comparable to that of the mr. For the given redshift interval it extends from $\dot{m}_{min} \approx 10^{-16} M_\odot/s$ up to $\dot{m}_{max} \approx 5 \times 10^{-6} M_\odot/s$. The mass corresponding to the lower accretion rate limit is $M_\bullet \approx 3 \times 10^5 M_\odot$ and the mass corresponding to the upper limit is $M_\bullet \approx 7 \times 10^8$. As for the mr resolution, the accretion rate stays below the Eddington limit. From Figure 2.2 again the formation of three individual groups in the whole population can be seen. The accretion rates of black holes within the intermediate mass range seem to be correlated to the redshift (see Figure 2.2). For redshifts larger than 0.3, the first group contains black holes having masses from $2 \times 10^5 M_\odot$ up to $10^6 M_\odot$ and having accretion rates from 0.01% up to 30% of the Eddington accretion rate. The intermediate mass range respectively the second group

contains black holes having masses from $10^6 M_\odot$ up to $2 \times 10^7 M_\odot$ and having accretion rate from 1% up to 100% of the Eddington accretion rate. The third group contains black holes having masses from $2 \times 10^7 M_\odot$ up to $10^{10} M_\odot$ and having accretion rates from 0.01% up to 1% of the Eddington accretion rate. For redshifts lower than z = 0.3, the lower limit of the accretion rate in the intermediate mass range is lower than 1%. of the Eddington accretion rate. I. e. the accretion rate in the intermediate mass range decreases for decreasing redshift. In Table 2.2 the characteristics for each of the three groups are once again given. These values are valid for redshifts larger than 0.3.

Table 2.2: Correlation of mass range and characteristic accretion rate (hr) ((1) Valid only for: $z > 0.3$)

Group	I	II	III
$M_\bullet/M_\odot$	$2 \times 10^5 - 10^6$	$10^6 - 2 \times 10^7$	$2 \times 10^7 - 10^{10}$
$\dot{m}/\dot{m}_{Edd}$	$10^{-4} - 0.3$	$0.01 - 1^1$	$10^{-4} - 0.01$

- **Ultra high resolution:** In this case, the redshift interval at which black holes are present expands from z = 6.81025 to z = 0.470194, and the mass reaches from $M_{\bullet,min} \approx 2 \times 10^4 M_\odot$ up to $M_{\bullet,max} \approx 2 \times 10^8 M_\odot$. In contrast to the mr and the hr, the existence of three groups is not evidently given, as it can be seen in Figure 2.3. Later on in the discussion, hints on the formation of three groups also in the uhr will be discussed, while at this point only two groups may be pointed out. The lowest accretion rate, $\dot{m}_{min} \approx 10^{-23} M_\odot/s$, corresponds to a black hole having a mass of $M_\bullet \approx 7 \times 10^4 M_\odot$, and the highest value for the accretion rate, $\dot{m}_{max} \approx 10^{-9} M_\odot/s$, corresponds to a black hole having a mass of $M_\bullet \approx 10^7 M_\odot$. Also for this resolution, there is no accretion with a larger value than the Eddington limit. The characteristics for this resolution are given in Table 2.3.

Table 2.3: Correlation of mass range and characteristic accretion rate (uhr).

Group	I	II
$M_\bullet/M_\odot$	$2 \times 10^4 - 2 \times 10^5$	$2 \times 10^5 - 2 \times 10^8$
$\dot{m}/\dot{m}_{Edd}$	$0 - 0.1$	$10^{-5} - \approx 1$

In order to compare the characteristics of the simulated AGNs with that of observed ones the mass ranges and the accretion rate ranges for the individual resolutions are

listed in Table 2.4. It is important to note that this comparison is more a rough estimate of the significance of the simulated findings than a statistical evaluation. Nevertheless, it is important for the discussion of the results. One problem for a well-founded evaluation would be the fact, that the accretion rate in Table 2.5 is only an estimate, because the bolometric luminosity has to be calculated under the assumption of isotropic radiation. Furthermore, the value for the efficiency is only an estimate.

From Table 2.5 we see, that the **mass range** of observed AGNs extends from 10^6 $M_\odot$ up to 3×10^9 $M_\odot$. In Subsection 1.1.3 the classification of black holes with regard to their masses was given. As a result, all black holes in observed AGNs seem to be SMBHs. While in the *uhr* the upper limit is not exceeded, in the *mr* and in the *hr* the heaviest black holes have masses up to 10^{10} $M_\odot$. This may be a result of the fact that the lowest redshift for the *uhr* is not 0.0 as for the *mr* and the *hr* but 0.470194. But note, that black holes having masses larger than $M_\bullet = 3 \times 10^9$ are already present for redshifts larger than z = 0.5 in the *mr* and the *hr*. Nevertheless, also for the *mr* and the *hr* the main part of the population has masses lower than 3×10^9 $M_\odot$. The occurrence of black holes with masses larger than $3 \times 10^9 M_\odot$ possibly results of difficulties according to the simulation of cooling processes leading to the existence of too massive black holes. Considering the lower limit of the lower masses points out, that in the *uhr* black holes occur with masses lower than 10^6 $M_\odot$, but accretion rates of more than $\dot{m} = 10^{-14} M_\odot/s$. According to their mass, these black holes may be classified as IMBHs, and according to their accretion rate they would be classified as AGNs (see Table 2.5). The presence of AGNs that contain IMBHs in the simulation in contrast to observations may be a result of anisotropic radiation. In particular, from Equation 1.34 it can be seen that the estimate of the lower mass limit depends on the luminosity. For anisotropic radiation this limit may increase, because the achievement of an equilibrium state would be possible also for lower masses for a given luminosity depending on the viewing direction. For the *mr* and the *hr*, all values for low masses are higher than 10^5 $M_\odot$.

For the observed AGNs, the **accretion rate** is calculated to take a value between 10^{-14} $M_\odot/s$ and 10^{-6} $M_\odot/s$ (see Table 2.5). For all resolutions in the simulation, the maximum values of the accretion rate are lower than or at least of the same order of magnitude as the observed upper limit and stay under the Eddington limit. The minimum values are for all resolutions lower than 10^{-14} $M_\odot/s$. As a result, the

Table 2.4: Mass ranges and accretion rate ranges for *mr*, *hr*, and *uhr*.

Resolution	mr	hr	uhr
$M_\bullet/M_\odot$	$10^6 \ - \ 10^{10}$	$2 \times 10^5 \ - \ 10^{10}$	$2 \times 10^4 \ - \ 2 \times 10^8$
$\dot{m}/(M_\odot/s)$	$10^{-16} \ - \ 10^{-6}$	$10^{-16} \ - \ 3 \times 10^{-6}$	$10^{-23} \ - \ 10^{-9}$

galaxies containing black holes with accretion rates lower than 10^{-14} $M_\odot/s$ would not be classified as active galaxies.

Table 2.5: Characteristics of AGNs as given in (Schneider, 2008). ((1) $L_\odot = 3.8 \times 10^{33} ergs/s$.; (2) $\dot{m}$, in this case, was calculated by using Equation 1.35, under the assumption $\epsilon = 0.1$ and with the approximation, that the whole luminosity in active galaxies is provided by the AGN.)

	Radio galaxies	Seyfert galaxies	QSOs	Blazars
$L/L_\odot{}^1$	$10^6 \ - \ 10^8$	$10^8 \ - \ 10^{11}$	$10^{11} \ - \ 10^{14}$	$10^{11} \ - \ 10^{14}$
$M_\bullet/M_\odot$	3×10^9	$10^6 \ - \ 10^9$	$10^6 \ - \ 10^9$	$10^6 \ - \ 10^9$
$\dot{m}/(\frac{M_\odot}{s})^2$	$10^{-14} \ - \ 10^{-12}$	$10^{-12} \ - \ 10^{-9}$	$10^{-9} \ - \ 10^{-6}$	$10^{-9} \ - \ 10^{-6}$

Figure 2.1: Medium resolution: Accretion rate (ordinate) and mass (abscissa) of the black holes together with the Eddington accretion rate (continuous line) for several redshifts, using logarithmic scaling.
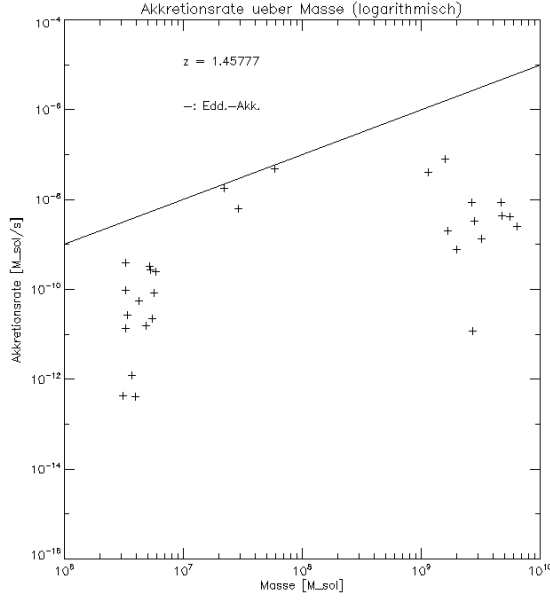

(a) z = 1.458
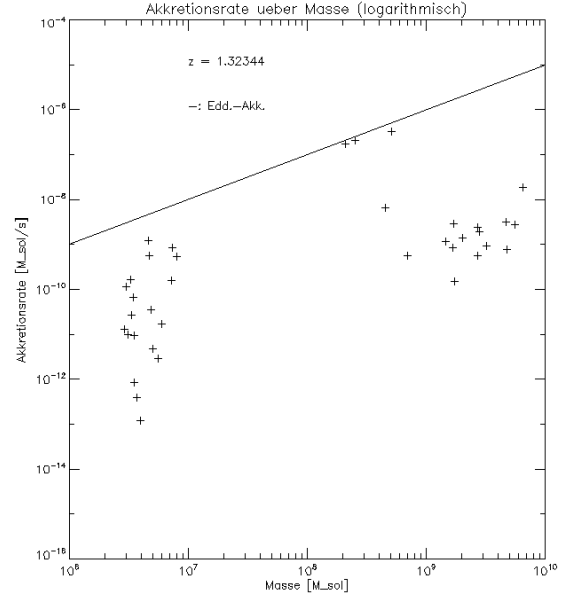
(b) z = 1.323
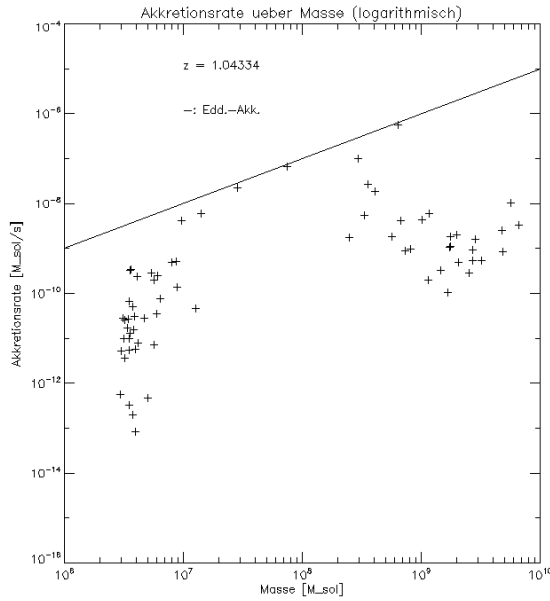
(c) z = 1.043
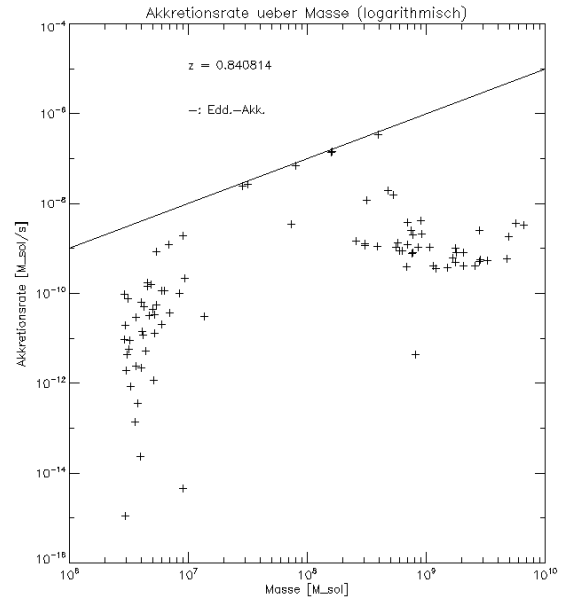
(d) z = 0.841
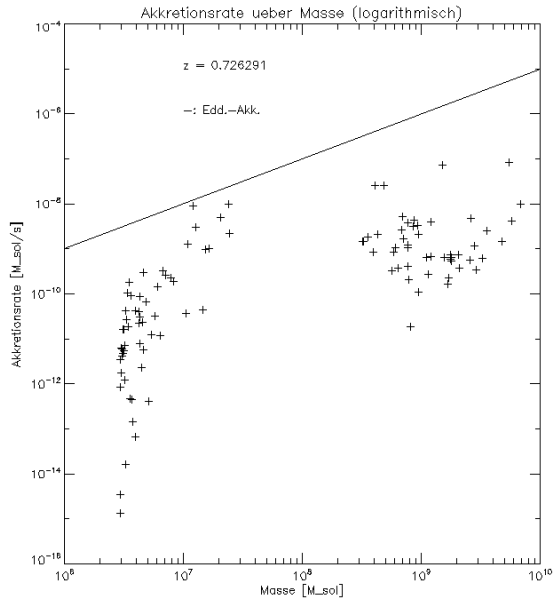
(e) z = 0.726
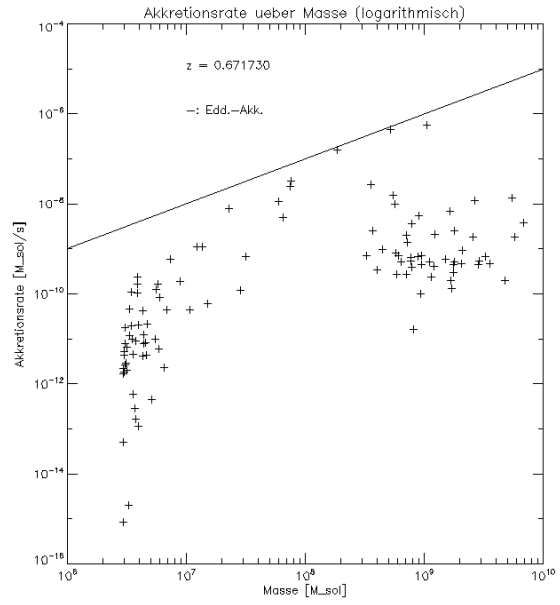
(f) z = 0.672
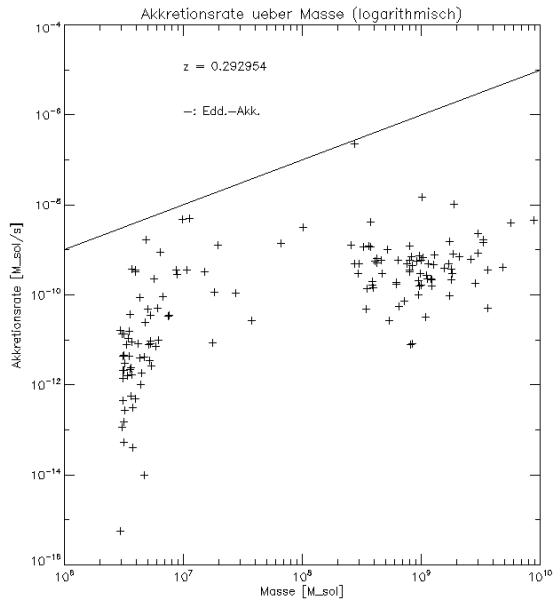
(g) z = 0.293
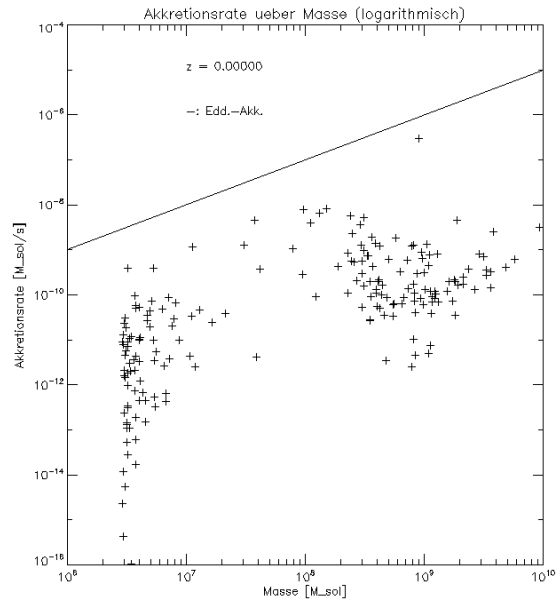
(h) z = 0.000

Figure 2.2: High resolution: Accretion rate (ordinate) and mass (abscissa) of the black holes together with the Eddington accretion (continuous line) rate for several redshifts, using logarithmic scaling.

(a) z = 1.980

(b) z = 1.706

(c) z = 1.179

(d) z = 0.841
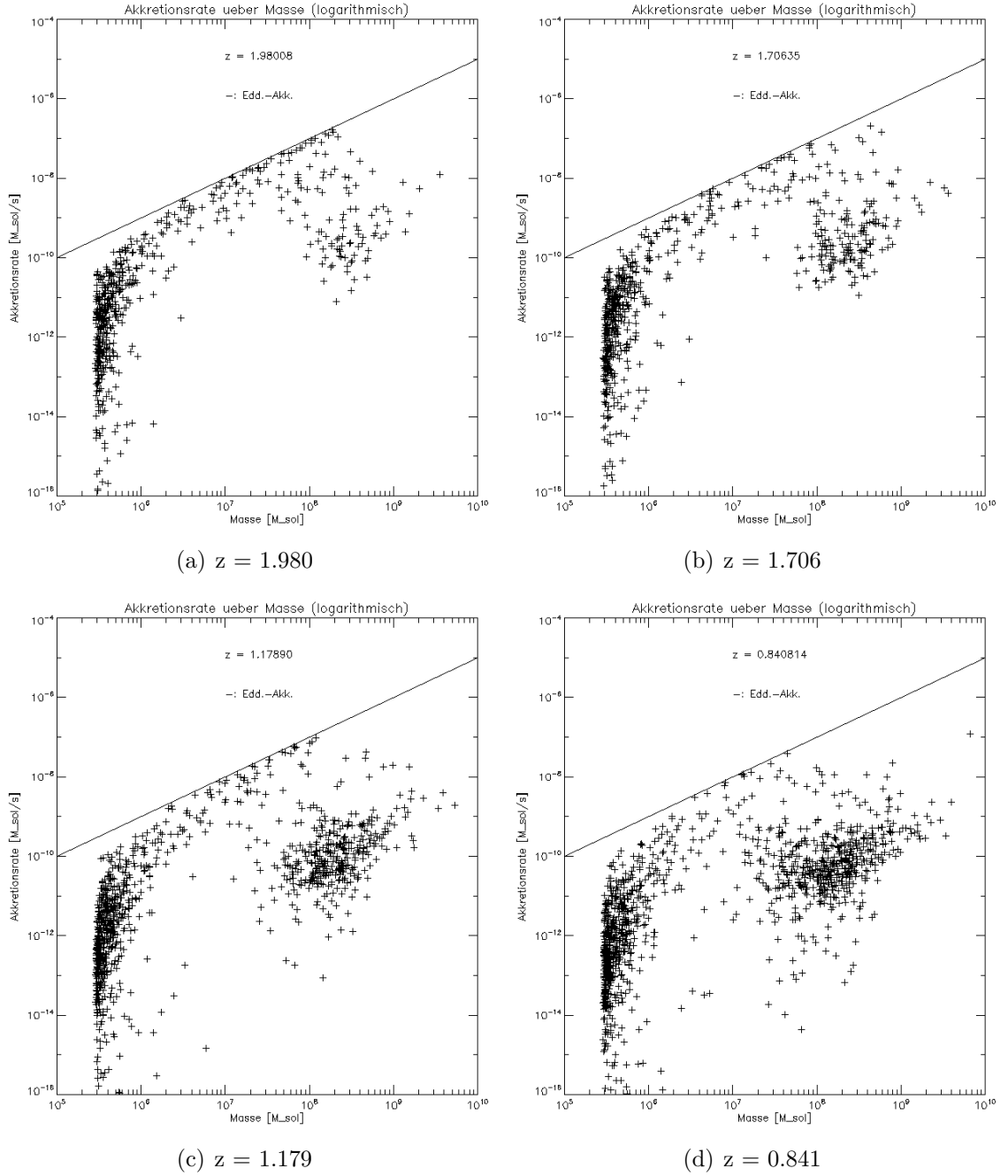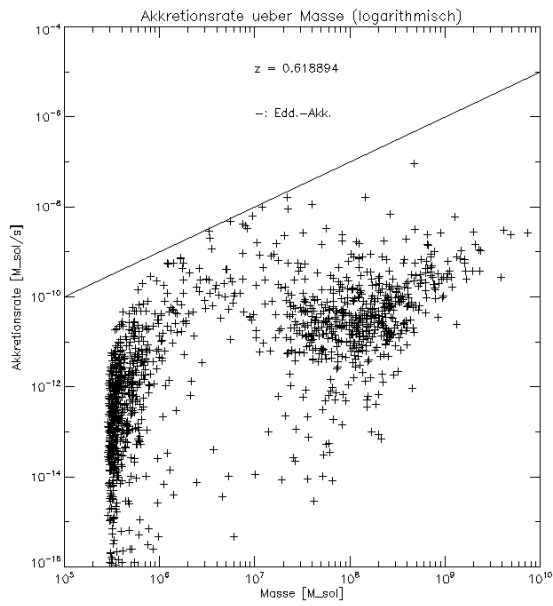
(e) z = 0.619
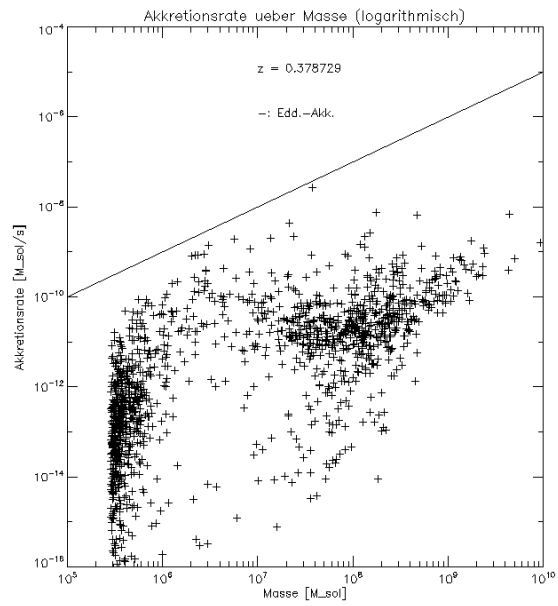
(f) z = 0.379
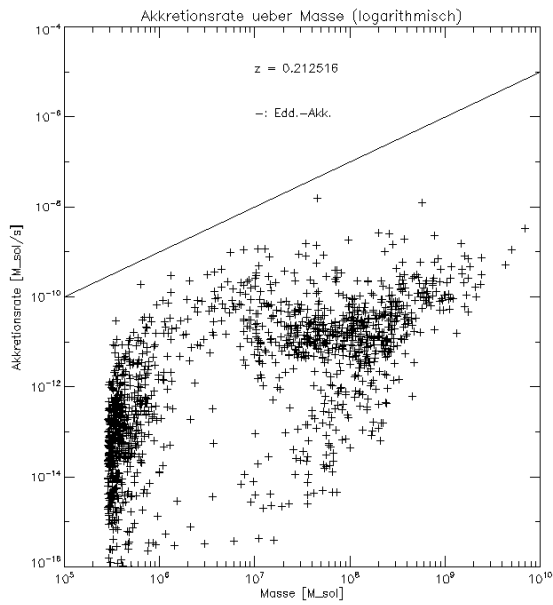
(g) z = 0.213
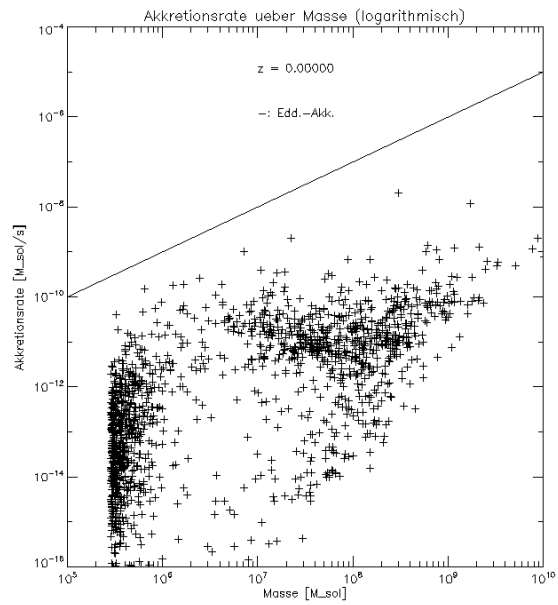
(h) z = 0.000

Figure 2.3: Ultra high resolution: Accretion rate (ordinate) and mass (abscissa) of the black holes together with the Eddington accretion rate (continuous line) for several redshifts, using logarithmic scaling.
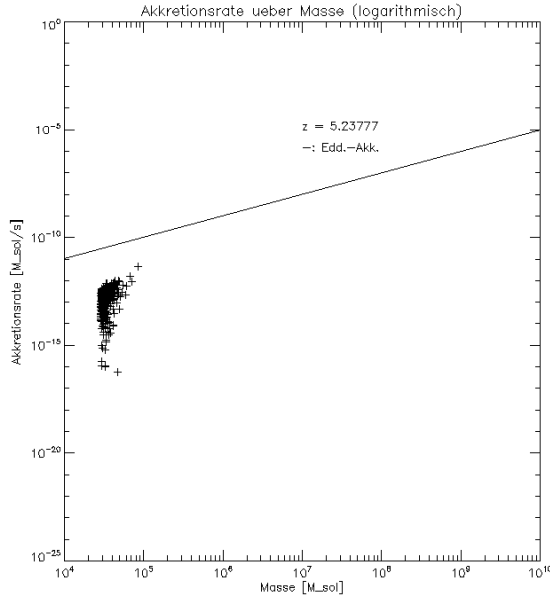
(a) z = 5.238
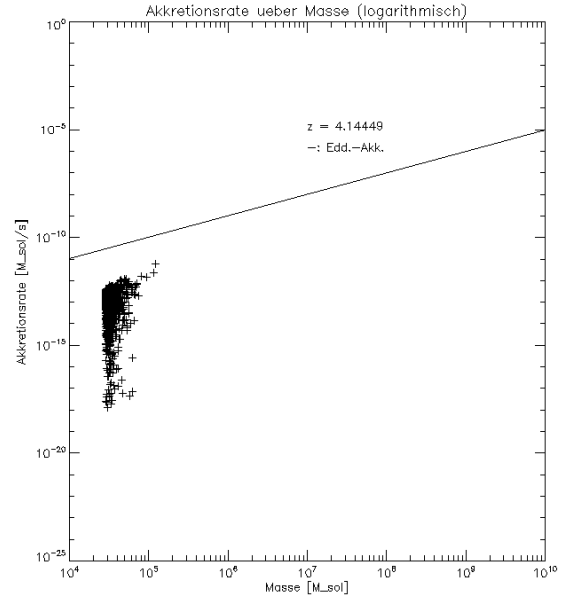
(b) z = 4.144
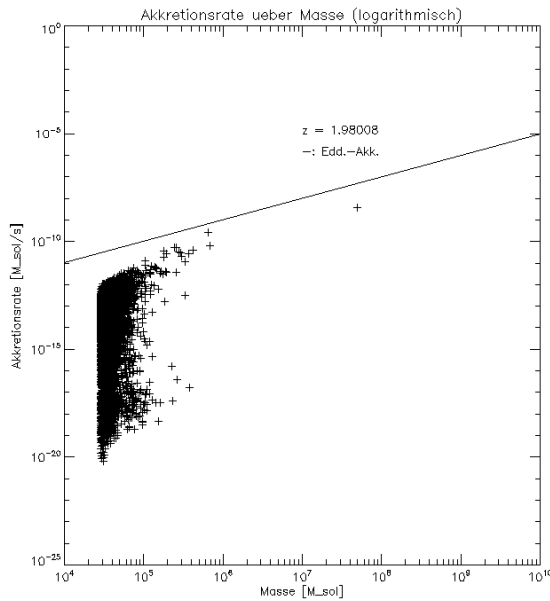
(c) z = 1.980
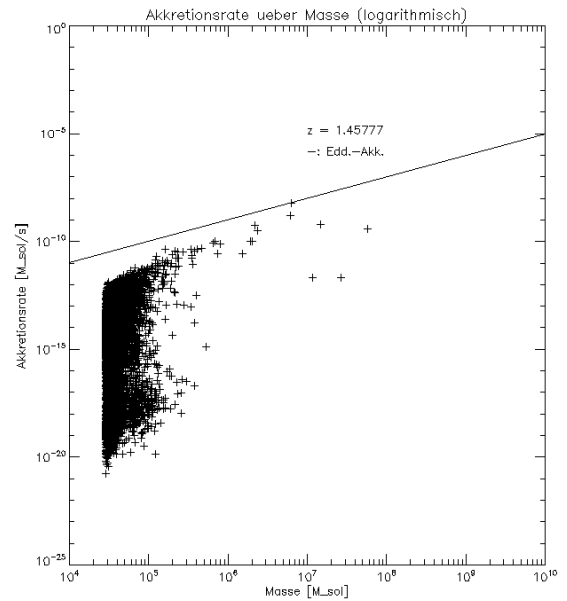
(d) z = 1.458
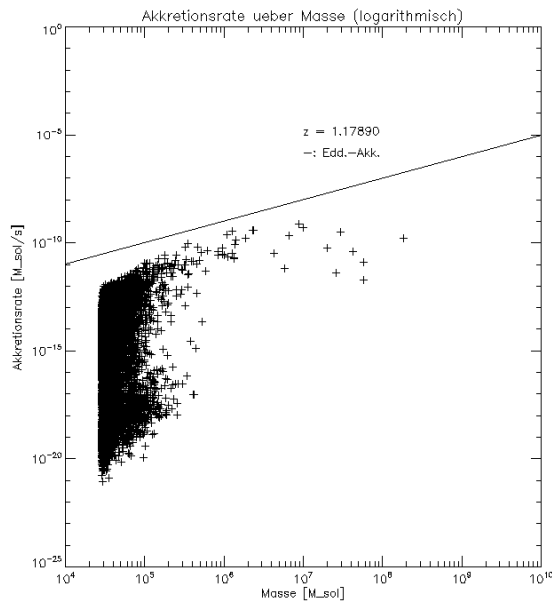
(e) z = 1.179
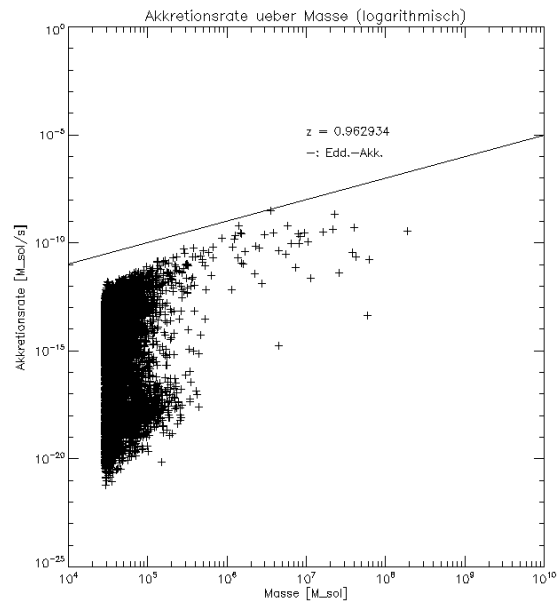
(f) z = 0.963
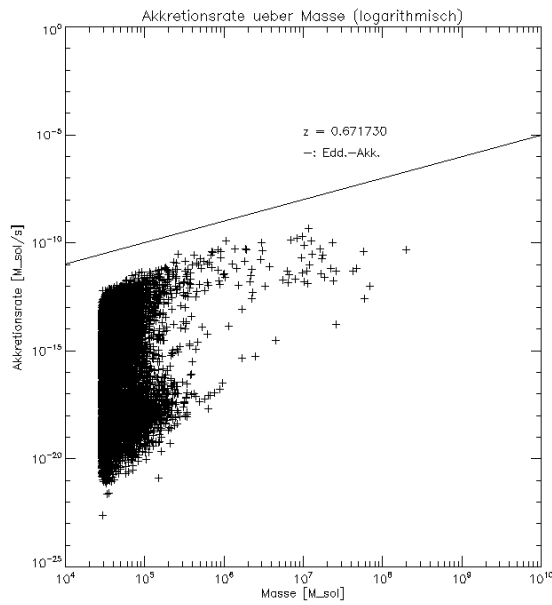
(g) z = 0.672
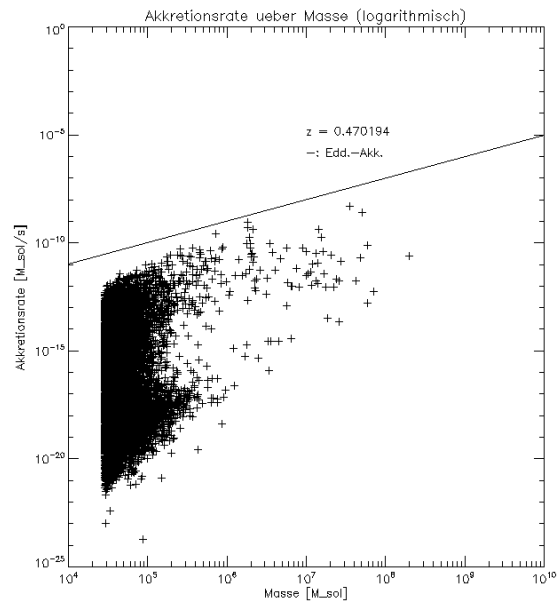
(h) z = 0.470

Discussion. In the description it was already mentioned, that in the *mr* and in the *hr* three mass ranges exist. The intermediate range may also be described as a gap. This gap separates the population into three groups, where two contain a high number of black holes. The group or gap in between contains less black holes than the other two groups. For the *uhr* this cannot be seen in Figure 2.3, but in Figure 2.7 at least a local minimum in the number of black holes per mass range may be detected. This minimum extends from $M_\bullet \approx 8 \times 10^4 \ M_\odot$ up to $M_\bullet \approx 2 \times 10^5 \ M_\odot$. In figures 2.5, 2.6, and 2.7 the number of black holes per mass range for the *mr*, the *hr*, and the *uhr* for several redshifts is given.

There is no way for black holes to loose mass. The only possible change in mass is a growth due to accretion. Because of the fact that for all simulated black holes at least a small accretion rate occurs, the change in mass has to be larger than zero for all black holes, i.e. $\Delta M_\bullet > 0$. The presence of three groups in the *mr* and in the *hr* and the minimum in the number per mass interval for all redshifts and in all resolutions in combination with a positive ΔM helps to analyze the typical behavior of the black holes. This behavior concerns the growth of mass and the characteristic accretion rate in the specific mass ranges. Thus it is correlated to the evolution of the accretion rate. One problem for the significance of the analyze is, that there is only a hint for the occurrence of three groups in the *uhr*, the minimum in the number per mass range (see figures 2.3 and 2.7). One more problem is the mentioned redshift-dependence of the typical accretion rate in the intermediate mass range for the *hr*.

Despite these problems, the typical behavior, which can be seen in figures 2.1 and 2.2, of the simulated black holes, at least in the *mr* and for redshifts larger than 0.3 also in the *hr*, seems to be as follows: The values for the accretion rates for black holes having a mass within the lowest mass range may take low and high values in reference to the Eddington accretion for this mass range. For most black holes having masses within the intermediate mass range the characteristic accretion rate is evidently larger in reference to the Eddington accretion rate for this mass range than in the low mass range. This leads to a faster growth of mass, than in the lower mass range. Black holes with masses belonging to the highest mass range again have lower characteristic accretion rates in reference to the Eddington accretion rate than in the intermediate mass range. This again leads to a slower growth of mass in the high mass range, than in the intermediate mass range. The combination of the different temporal behavior concerning the growth of mass leads to the forming of

Table 2.6: Calculated time slices for the individual resolutions.

Resolution	$\Delta M_\bullet/M_\odot$	$\Delta t_{cal}/yr$
mr	9×10^7	8×10^8
hr	9×10^6	8×10^8
uhr	9×10^6	4×10^8

a minimum in the number per mass range.

In order to check these assumptions concerning the behavior, the time slices for the evolution within the intermediate mass range in the simulation should be compared with calculated ones. The calculation of the time slice t_{cal} was done with the help of equations 1.37 and 1.38. Equation 1.38 can be transformed into:

$$\Delta t_{cal} = \frac{\Delta M_\bullet}{\dot{m}'}, \tag{2.1}$$

where $\dot{m}'$ is an approximation for the mean accretion rate within the investigated mass interval $\Delta M_\bullet$. In particular, it was calculated by the following equation:

$$\dot{m}' = 0.1 \times 0.5 \times (\dot{m}_{edd}(M_{\bullet,l}) + \dot{m}_{edd}(M_{\bullet,u})), \tag{2.2}$$

where $M_{\bullet,l}$ and $M_{\bullet,u}$ stand for the lower respectively for the upper limit of the intermediate mass range, 0.1 occurs in order to estimate the percentage of the accretion rate as a function of the Eddington accretion, and 0.5 determines the middle of the mass interval. The efficiency used for the calculation of the Eddington accretion rate is 0.1. The calculated time slices for the increase of mass leading to the crossing of the intermediate mass range are given for the individual resolutions in Table 2.6 in combination with the corresponding mass interval.

The typical time for the crossing of the intermediate mass range is exemplary determined by the analysis of Figure 2.4. This figure shows diagrams of the same structure as shown in Figure 2.1, but for directly succeeding snapshots. In the second and third figure, three black holes are marked. It seems likely to assume the marked group of three black holes at redshift z = 1.458 to correspond to the marked group at redshift z = 1.323.

In this case, it was possible to observe the evolution of a group. Because this is not possible in many cases, when using diagrams as shown in figures 2.1 and 2.4, the time slices have to be gained without observing individual black holes. In order

Figure 2.4: Medium resolution: Accretion rate (ordinate) and mass (abscissa) of the black holes together with the Eddington accretion rate (continuous line) for directly succeeding snapshots, using logarithmic scaling.


(a) z = 1.706   (b) z = 1.458   (c) z = 1.323
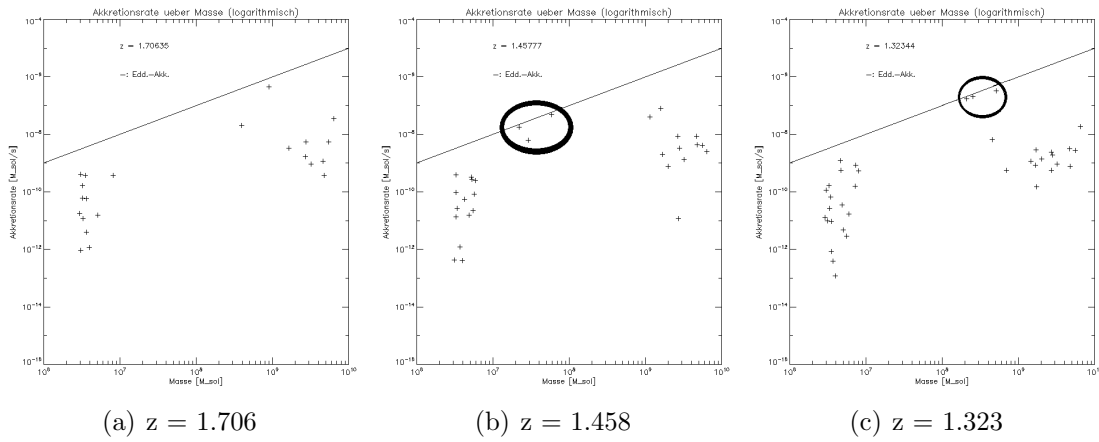
Table 2.7: Index of snapshots, redshift, and corresponding time using data from *mr*.

	Snapshot	Redshift z	time/Gyr
from	040	1.706	2.11
to	048	1.323	2.65
from	072	0.783	3.94
to	088	0.568	4.78
from	116	0.252	6.70
to	124	0.174	7.38

to do this, one can note the redshift for two snapshots, where no or a small number of black holes occur in the intermediate mass range. At least one snapshot has to be given in between, containing many black holes in this range. As a result of the occurrence of black holes in the intermediate mass range for a redshift between the two noted redshifts, one can assume, that these black holes have crossed the intermediate mass range in the corresponding redshift interval. The redshift can be transformed into time by using Equation 1.14. In Table 2.7 the indices of the snapshots, the redshift, and the corresponding time are listed for the *mr*.

Using the values listed in Table 2.7 we calculated, that it takes a black holes between 5×10^8 yr and 8×10^8 yr to cross the intermediate mass range. This is comparable at least in the order of magnitude to the time slices, calculated for each redshift, listed in Table 2.6. This in combination with the positive $\Delta M_\bullet$ is

consistent with the assumption, that in most cases a period of high accretion rates exists following on a period of low accretion rates and again being followed by a period of low accretion rates, when black holes transfer from the low mass range to the high mass range because of accretion. Additionally to the fact, that the number of black holes occurring in the intermediate mass range is lower than in the other ranges, most black holes in this range seem to belong to AGNs.

Figure 2.5: Medium resolution: Number of BHs per mass interval (ordinate) and mass interval (abscissa) for several redshifts.
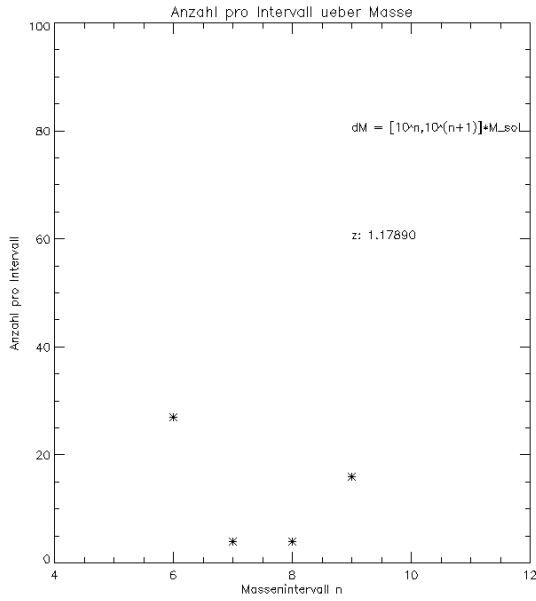
(a) z = 1.179
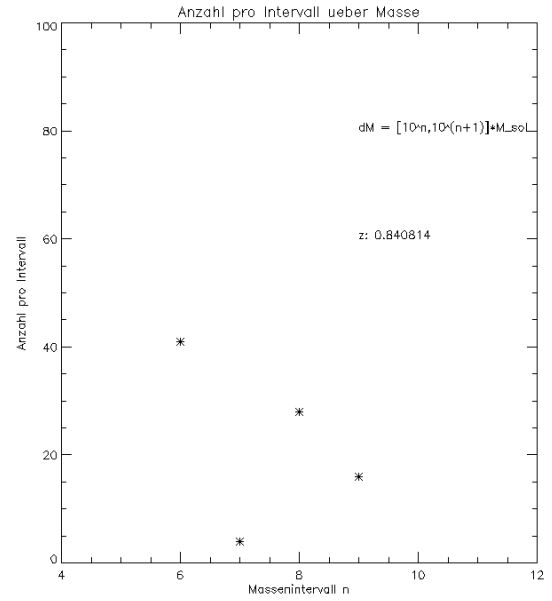
(b) z = 0.841
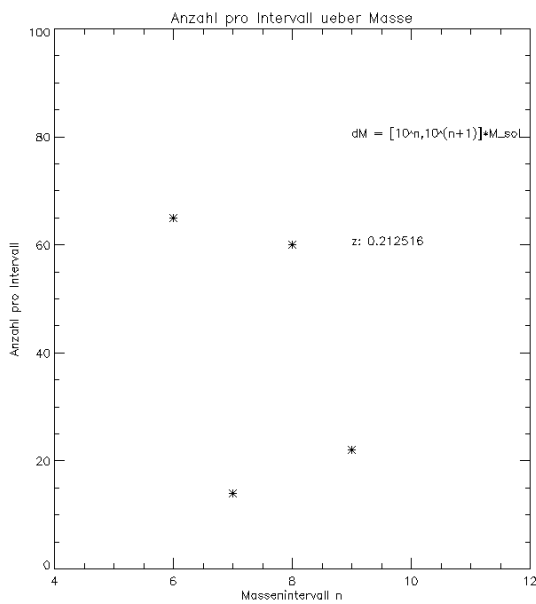
(c) z = 0.213
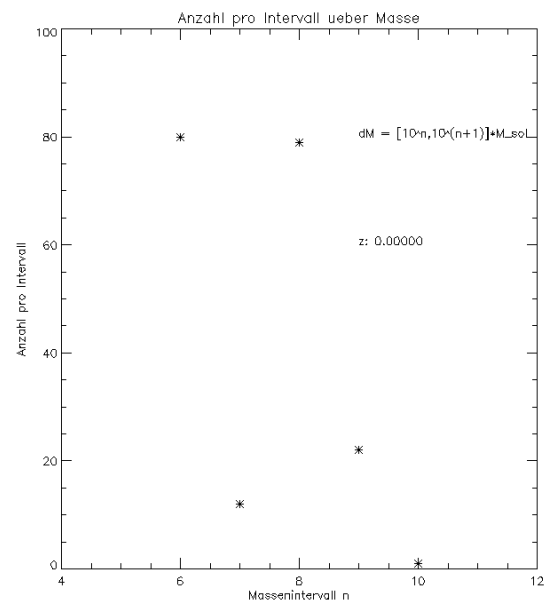
(d) z = 0.000

Figure 2.6: High resolution: Number of BHs per mass interval (ordinate) and mass interval (abscissa) for several redshifts, using logarithmic scaling.
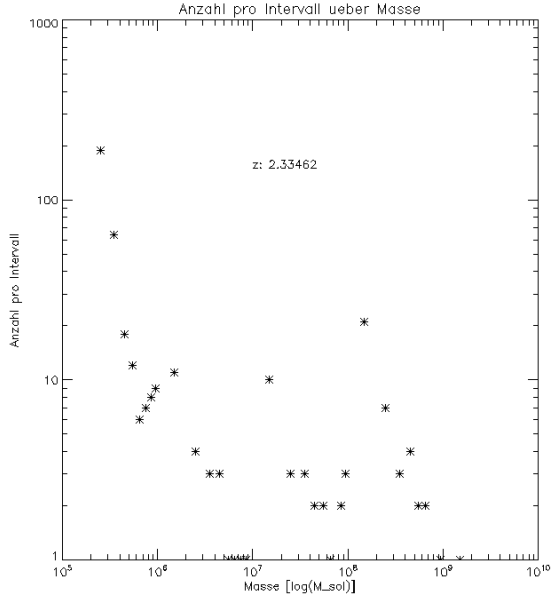
(a) z = 2.335
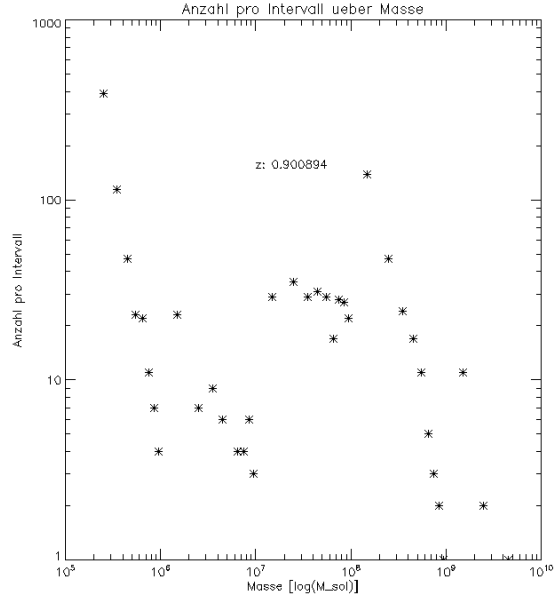
(b) z = 0.901
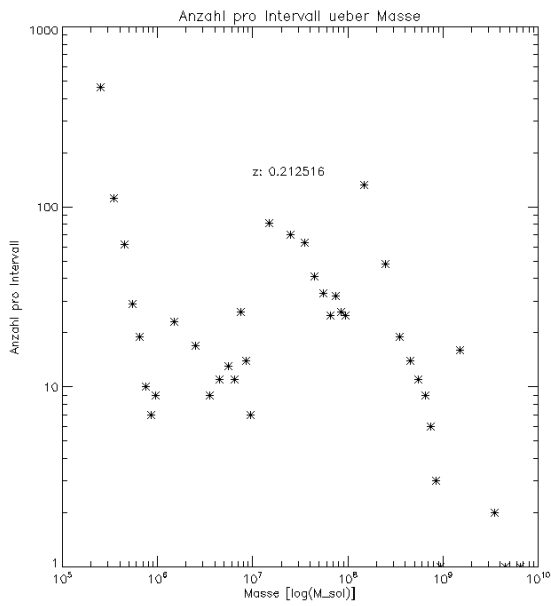
(c) z = 0.213
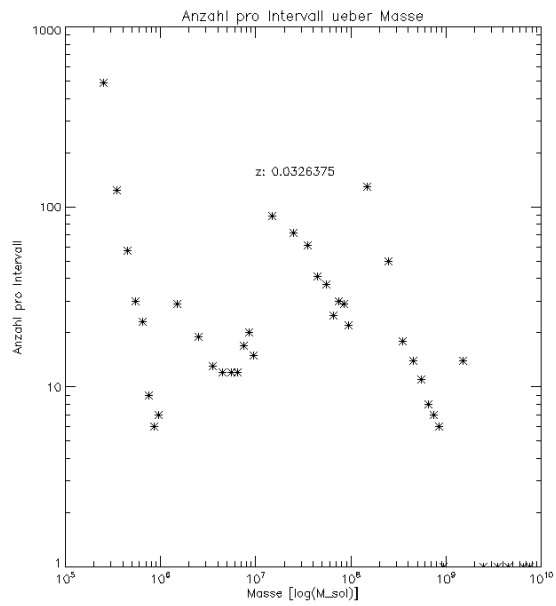
(d) z = 0.033

Figure 2.7: Ultra high resolution: Number of BHs per mass interval (ordinate) and mass interval (abscissa) for several redshifts, using logarithmic scaling.
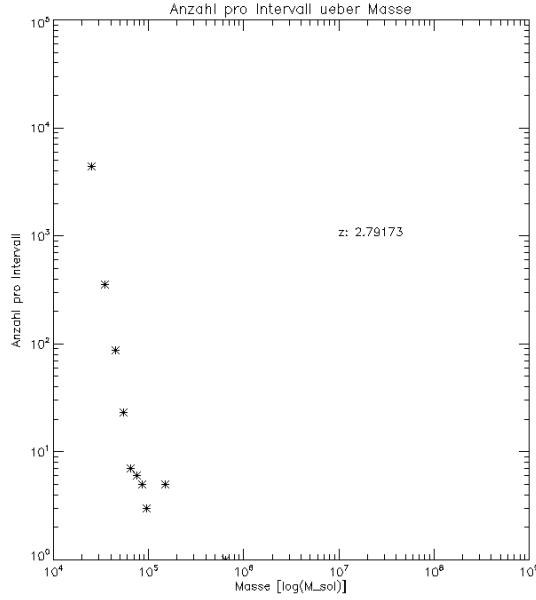
(a) z = 2.791
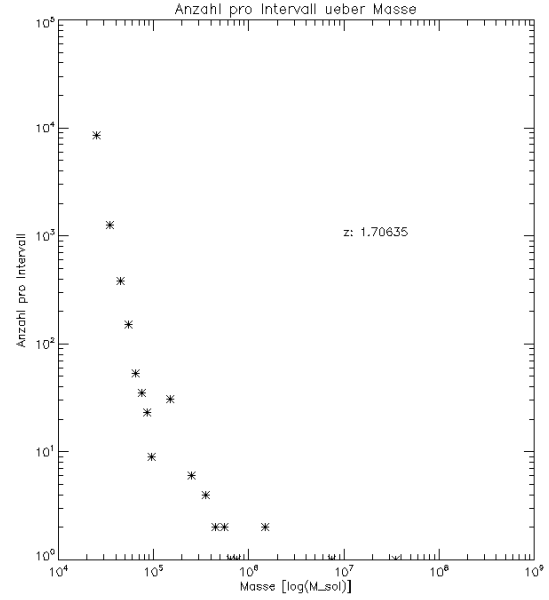
(b) z = 1.706
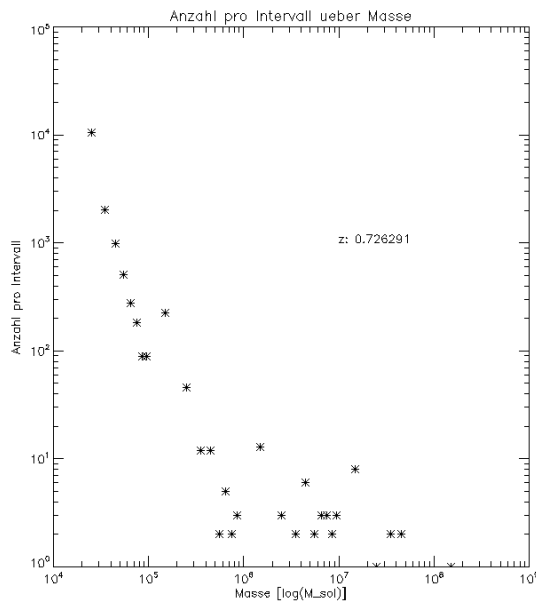
(c) z = 0.726
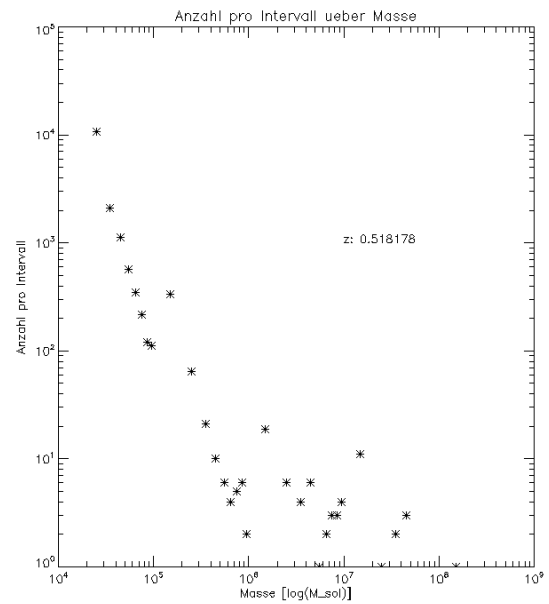
(d) z = 0.518

2.2.2 Luminosity function

In order to investigate, which range of the accretion rate has high accuracy in the simulation respectively which range describes observable phenomena best, once again a comparison with observational data should be done. This classification of simulated accretion helps to estimate the validness of the assumptions, made in Subsection 2.2.1 concerning the evolution of mass and especially of the accretion rate. Nevertheless, only statements concerning the absolute number per luminosity interval respectively accretion rate interval may be given by the comparison concerning the luminosity function as a result of its definition. Thus no statements concerning the composition of black holes per mass range are possible.

In this subsection, the calculated bolometric luminosity function is compared to the luminosity function, described by Equation 1.42 for optical wavelength range. As mentioned in Subsection 1.2.4, Equation 1.42 was gained by fitting observational data with parameters given in Table 1.2. Here the calculation of the bolometric luminosity function for simulated data was done by using Equation 1.40. The luminosity intervals dL are marked by an index n and calculated to be $dL = [10^n \times 10^{37} ergs/s, 10^{n+1} \times 10^{37} ergs/s]$ with $n \in 0, 1, ..., 12$ (see figures 2.8, 2.9, and 2.10). The expansion of space was taken into account by using the following equation:

$$V = \frac{a^3}{(z+1)^3},$$ (2.3)

where $a = 48 Mpc/h$ corresponds to the edge length of the considered box. In figures 2.8, 2.9, and 2.10 the luminosity function is plotted as a function of the luminosity with the luminosity separated in intervals marked by n as described above. The continuous line represents the fitted luminosity function and the crosses represent the calculated one. In order to come to the accretion rate intervals, the luminosity was converted into an accretion rate by using Equation 1.35.

Because of the resolution-dependence of the data, the comparison is once again done for every resolution separately. It is important to note, that for the fitted luminosity function only observational data for one type of AGNs (QSOs) were taken into account. As a result, the calculated luminosity function for the simulation might take higher values than the fitted one. This was taken into account when looking for luminosity intervals where simulated data reproduce observations. I. e. when the calculated luminosity function has higher values than the fitted one, the

corresponding intervals were rather taken as reproducing the observation, than intervals, where the calculated luminosity function has lower values, than the fitted one, because for the fitted one only QSOs and for the calculated one all types of AGNs were taken into account. The first two intervals in figures 2.8, 2.9, and 2.10 contain black holes with luminosities lower than $10^{39} erg/s$. As a result, these black holes would not be classified as belonging to an AGN (see Table 2.5).

- **Medium resolution.** From Figure 2.8 we see the calculated luminosity function to be in good agreement with the fitted one for the intervals $n = 5$ and $n = 6$ for all redshifts. In Table 2.8 the redshift, the luminosity interval and the accretion rate interval are given. It turns out, that in the simulation the luminosity interval extending from $L = 10^{42} erg/s$ to $L = 10^{44} erg/s$ describes the observational data best. This luminosity interval corresponds to an accretion rate interval from $\dot{m} = 6 \times 10^{-12} M_\odot/s$ to $\dot{m} = 6 \times 10^{-10} M_\odot/s$. For lower luminosities the calculated luminosity function has lower values than the fitted one, and for higher luminosities, the calculated one has higher values than the fitted one. I. e., the absolute number of simulated black holes in these luminosity ranges does not fit with observations, because the luminosity function is correlated to the number of black holes per comoving volume element and luminosity interval as it can be seen form Equation 1.40.

Table 2.8: Luminosity and accretion rate interval for the best description of observed data by the simulation (mr).

Redshift	Luminosity/(erg/s)	Accretion rate/$(M_\odot/s)$
$3.38 - 0.00$	$10^{42} - 10^{44}$	$6 \times 10^{-12} - 6 \times 10^{-10}$

- **High resolution.** The luminosity range reproducing observational data in the simulation in this case seems to depend on the redshift. In Table 2.9 the different ranges are given with corresponding redshift interval. Figure 2.9 shows a diagram for each redshift interval. From Table 2.9 we see, that the luminosity intervals respectively the accretion rate intervals describing observations best shift to higher values and become wider as a function of redshift. The broadest range extends from $10^{41} erg/s$ to $10^{45} erg/s$ for redshifts between z = 3.38 and z = 1.81. This corresponds to accretion rates extending from $\dot{m} = 6 \times 10^{-13} M_\odot/s$ to $\dot{m} = 6 \times 10^{-9} M_\odot/s$. As for the mr, the calculated luminosity function for low luminosities has lower values than the fitted one,

while for high luminosities the calculated one has higher values than the fitted one.

Table 2.9: Luminosity and accretion rate interval for the best description of observed data by the simulation in dependence of the redshift (hr).

Redshift	Luminosity/(erg/s)	Accretion rate/$(M_\odot/s)$
$3.38 - 1.81$	$10^{38} - 10^{40}$	$6 \times 10^{-16} - 6 \times 10^{-14}$
$1.80 - 0.75$	$10^{39} - 10^{42}$	$6 \times 10^{-15} - 6 \times 10^{-12}$
$0.74 - 0.71$	$10^{40} - 10^{43}$	$6 \times 10^{-14} - 6 \times 10^{-11}$
$0.70 - 0.00$	$10^{41} - 10^{45}$	$6 \times 10^{-13} - 6 \times 10^{-9}$

- **Ultra high resolution.** From Figure 2.10 we find the luminosity range describing observational data best to depend on redshift. In Table 2.10 the luminosity intervals and the accretion rate intervals are listed with the corresponding redshift. The characteristics concerning the differences between calculated and fitted luminosity function vary in comparison to the mr and the hr. In this case, no typical discrepancy for high and low luminosities exists. It turns out, that the difference seems to depend on the redshift. For redshift larger than z = 0.73 most of the simulated values are higher than the observed ones, and for redshifts lower than z = 0.73 most of the simulated values are lower than the observed ones.

Table 2.10: Luminosity and accretion rate interval for the best description of observed data by the simulation in dependence of the redshift (uhr).

Redshift	Luminosity/(erg/s)	Accretion rate/$(M_\odot/s)$
$3.00 - 0.74$	$10^{42} - 10^{45}$	$6 \times 10^{-14} - 6 \times 10^{-9}$
$0.73 - 0.40$	$10^{39} - 10^{45}$	$6 \times 10^{-15} - 6 \times 10^{-9}$

Discussion. The comparison of the calculated luminosity function for the simulation with the fitted one, gained by fitting observational data, pointed out accretion rate ranges for each resolution describing observational data best. By comparing the accretion rate intervals given in Table 2.8 with the overall accretion rate shown in Figure 2.8 for the mr we see, that the simulation provides high accuracy in an accretion rate range excluding accretion rates larger than $\dot{m} = 6 \times 10^{-10} M_\odot/s$ and lower than $\dot{m} = 6 \times 10^{-12} M_\odot/s$. For redshifts higher than 0.7 we come to a similar

statement for the hr for high accretion rates by comparing the accretion rate ranges given in Table 2.9 with the overall accretion rate shown in Figure 2.9. The upper limit in this case depends on the redshift as shown in Table 2.9. For redshifts lower than 0.7 high accuracy is given for high accretion rates up to $\dot{m} = 6 \times 10^{-9} M_\odot/s$, but not for low accretion rates lower than $\dot{m} = 6 \times 10^{-13} M_\odot/s$. The comparison of the accretion rate ranges given in Table 2.10 with the overall accretion rate shown in Figure 2.10 point out high accuracy in the uhr for accretion rate larger than $\dot{m} = 6 \times 10^{-14} M_\odot/s$ respectively $\dot{m} = 6 \times 10^{-15} M_\odot/s$ depending on the redshift.

In general, inaccuracies in the description of black holes having low luminosities respectively low accretion rates may result of the resolution. This can be seen by comparing the lower limit of the accretion rate range providing high accuracy given in Table 2.8 for the mr with the lower limits given in Table 2.9 for the hr.

Figure 2.8: Medium resolution: Luminosity function (ordinate, using logarithmic scale) and luminosity interval (abscissa) for several redshifts, the continuous line represents the fitted luminosity function and the crosses represent the calculated one.
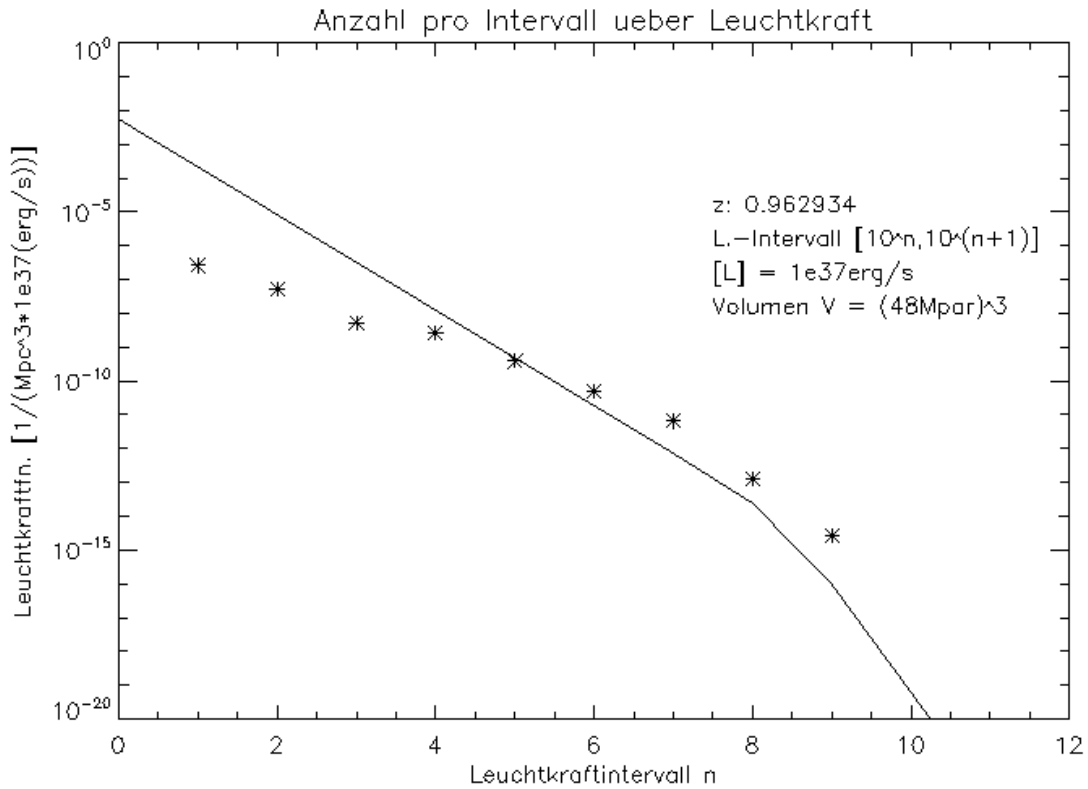

(a) z = 0.962
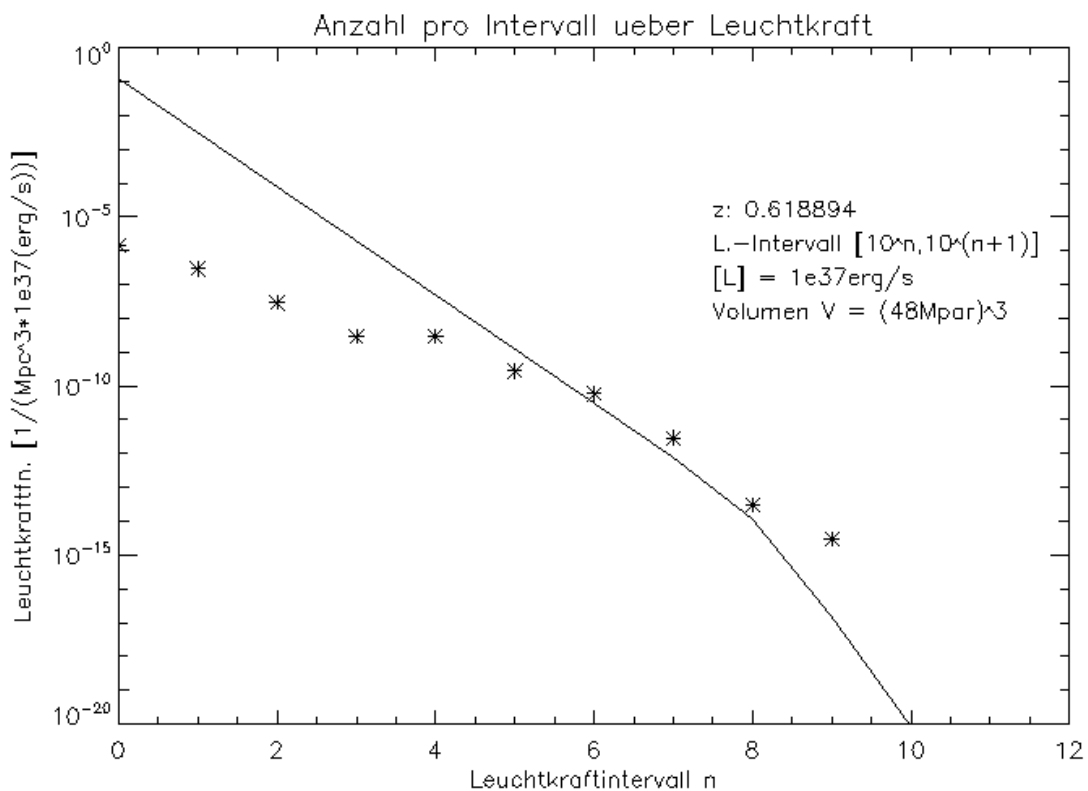
(b) z = 0.619
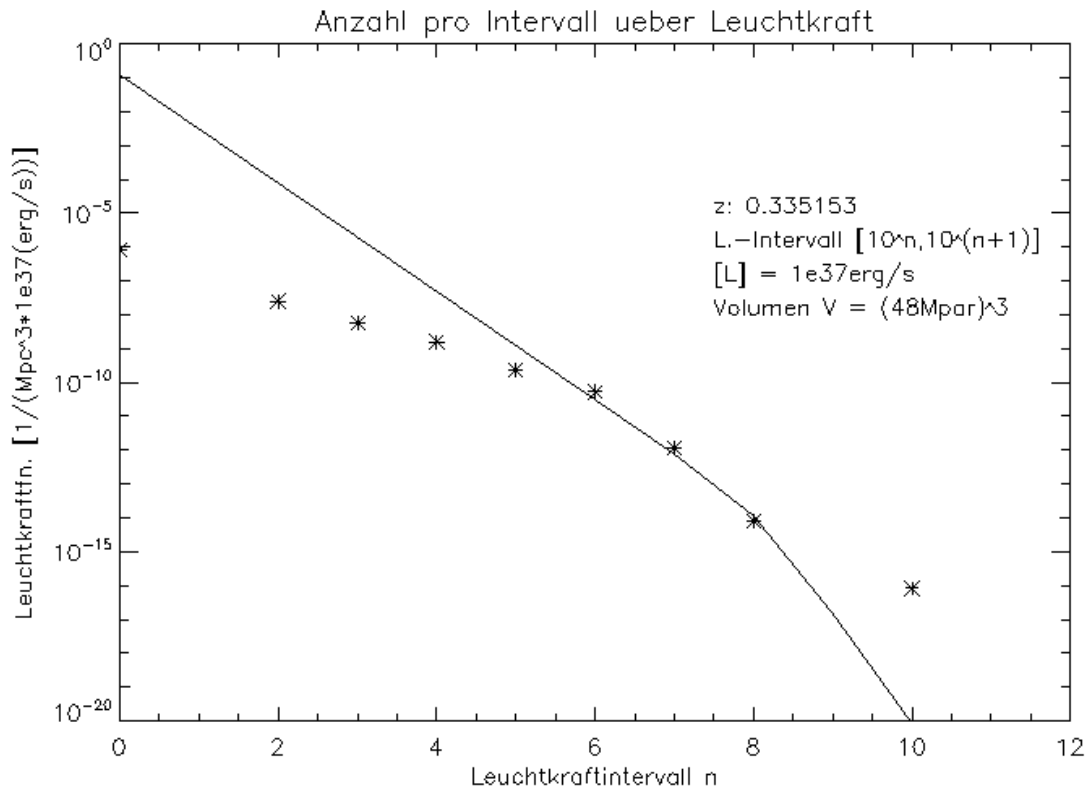
(c) z = 0.335
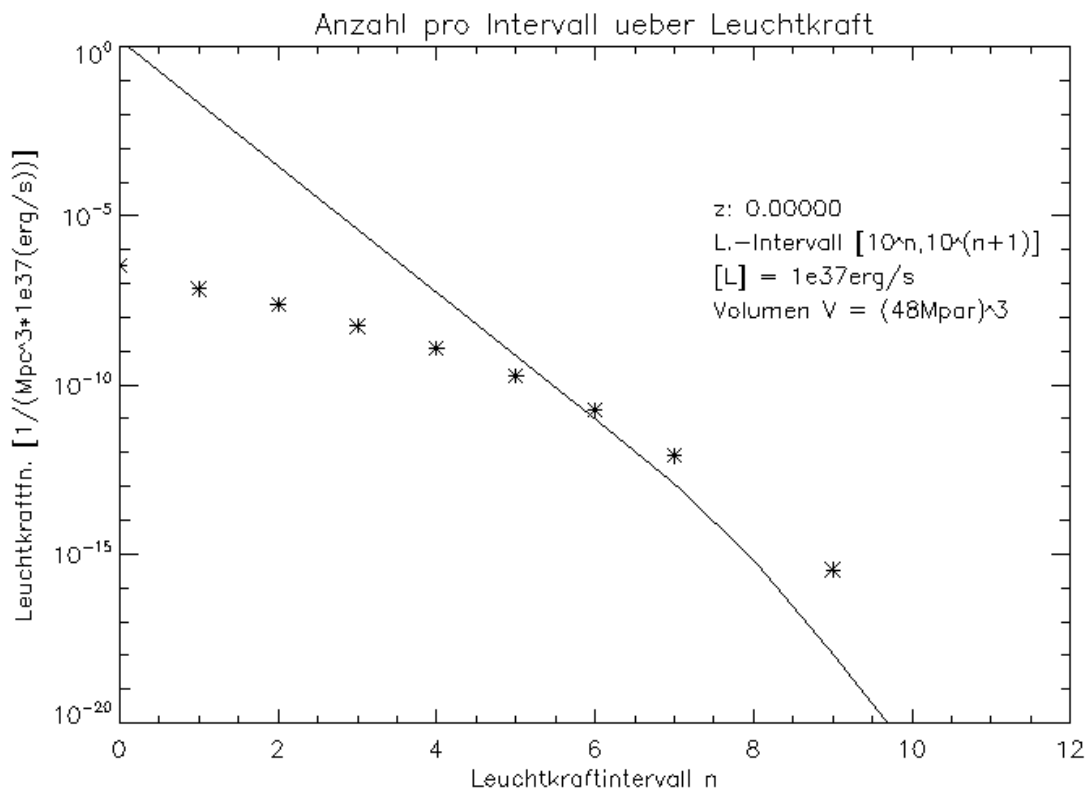
(d) z = 0.000

Figure 2.9: High resolution: Luminosity function (ordinate, using logarithmic scale) and luminosity interval (abscissa) for several redshifts, the continuous line represents the fitted luminosity function and the crosses represent the calculated one.
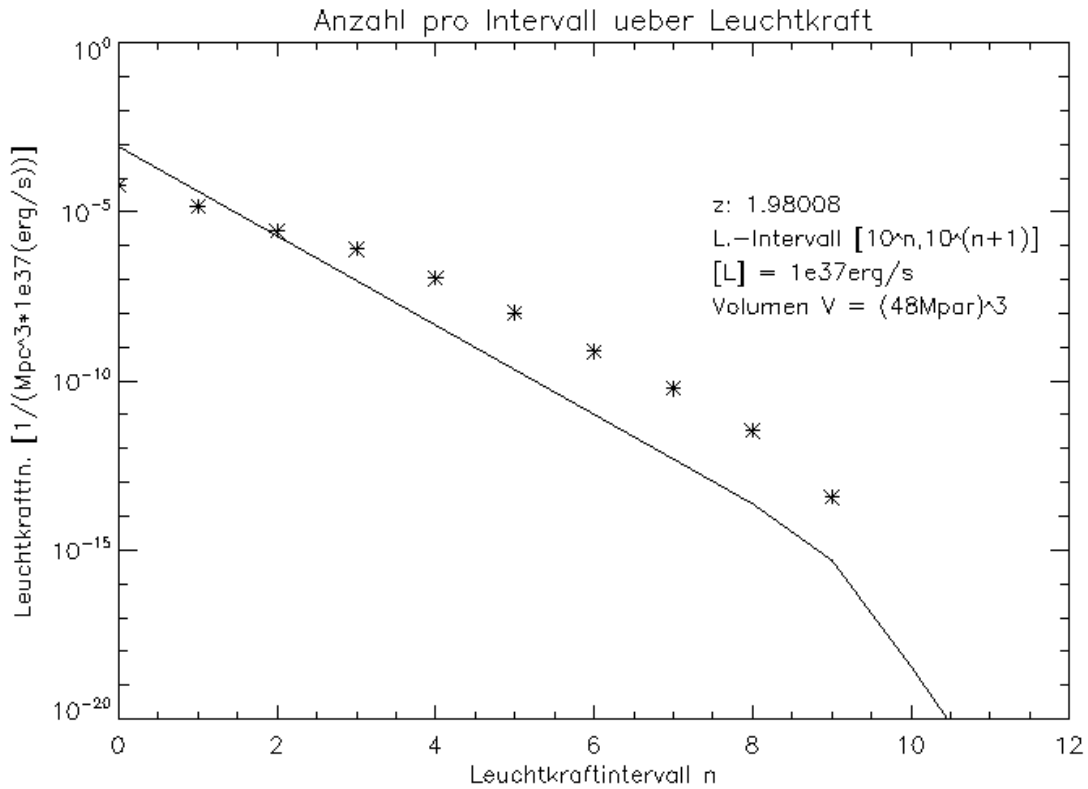

(a) z = 1.980
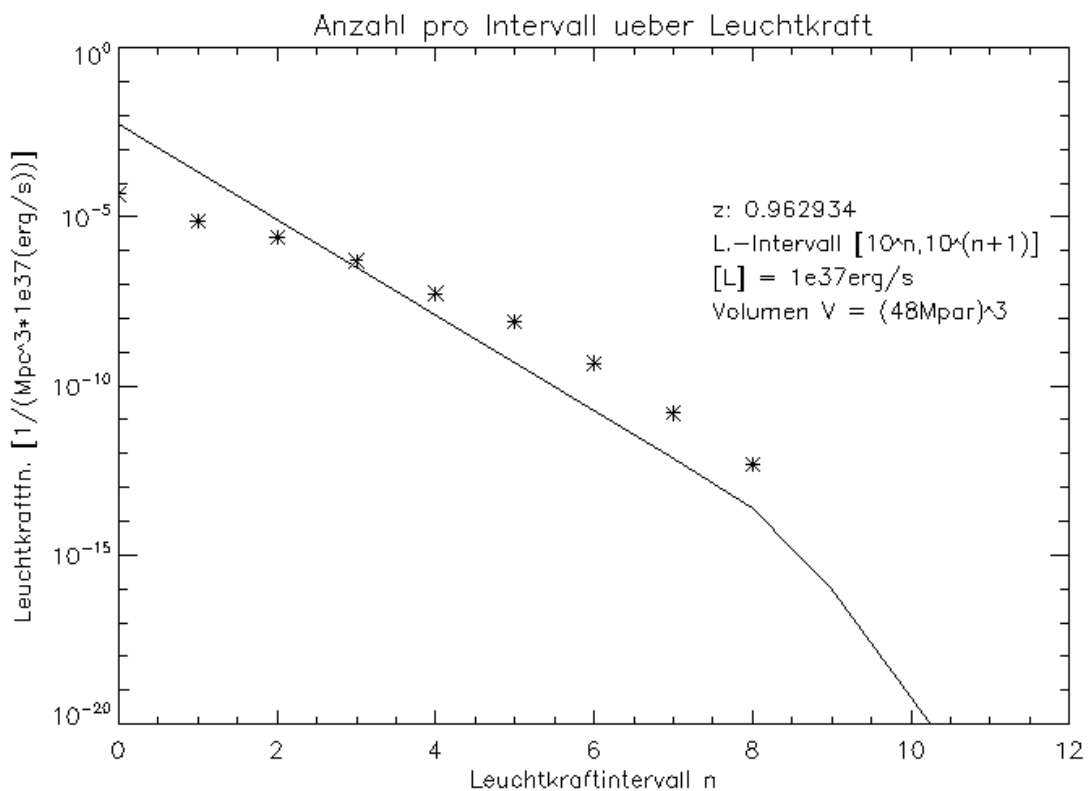
(b) z = 0.963
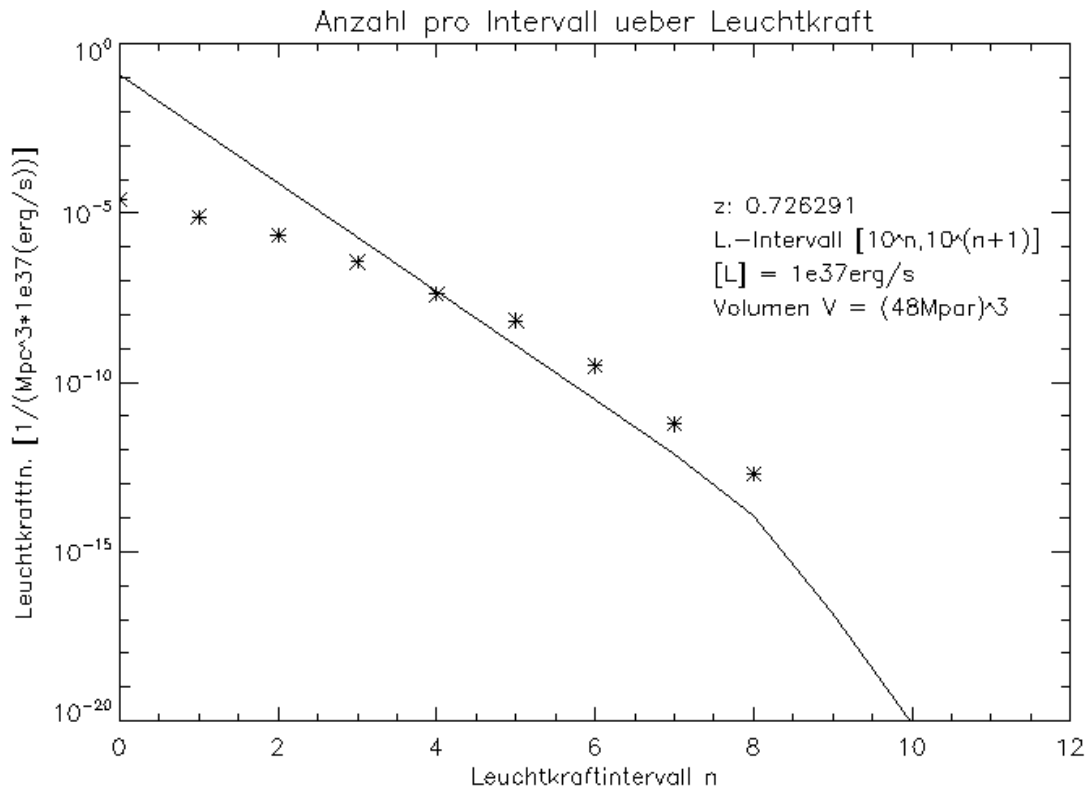
(c) z = 0.726
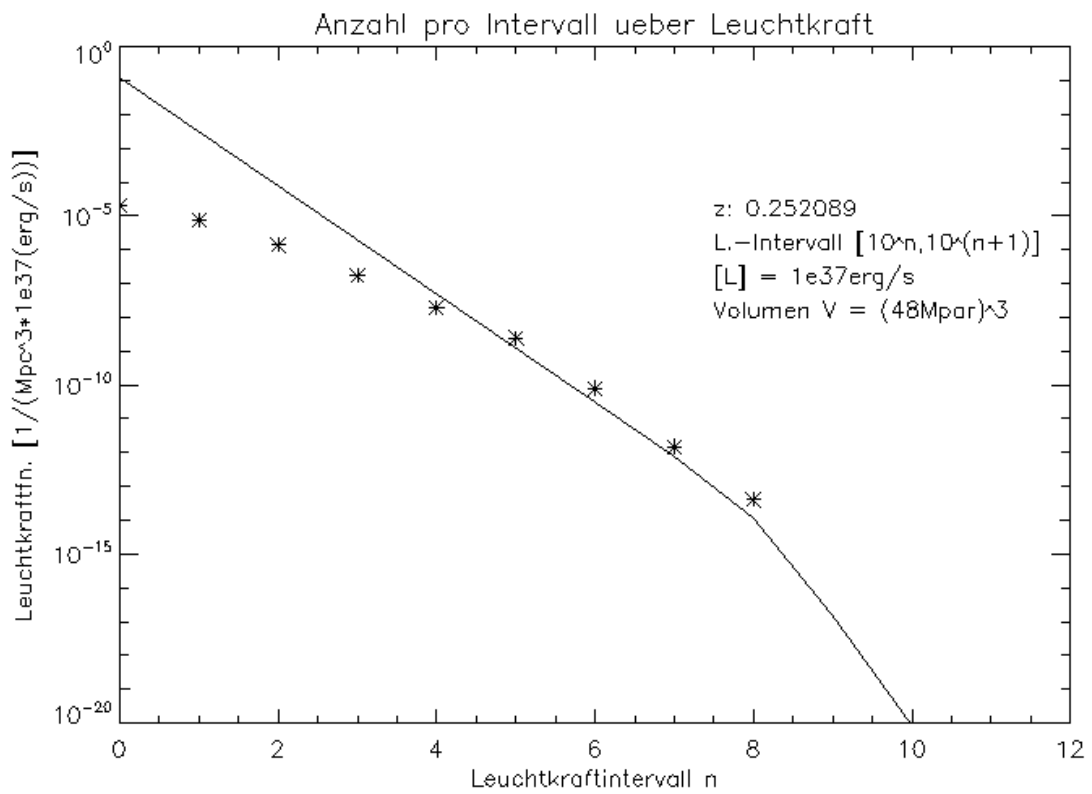
(d) z = 0.252

Figure 2.10: Ultra high resolution: Luminosity function (ordinate, using logarithmic scale) and luminosity interval (abscissa) for several redshifts, the continuous line represents the fitted luminosity function and the crosses represent the calculated one.
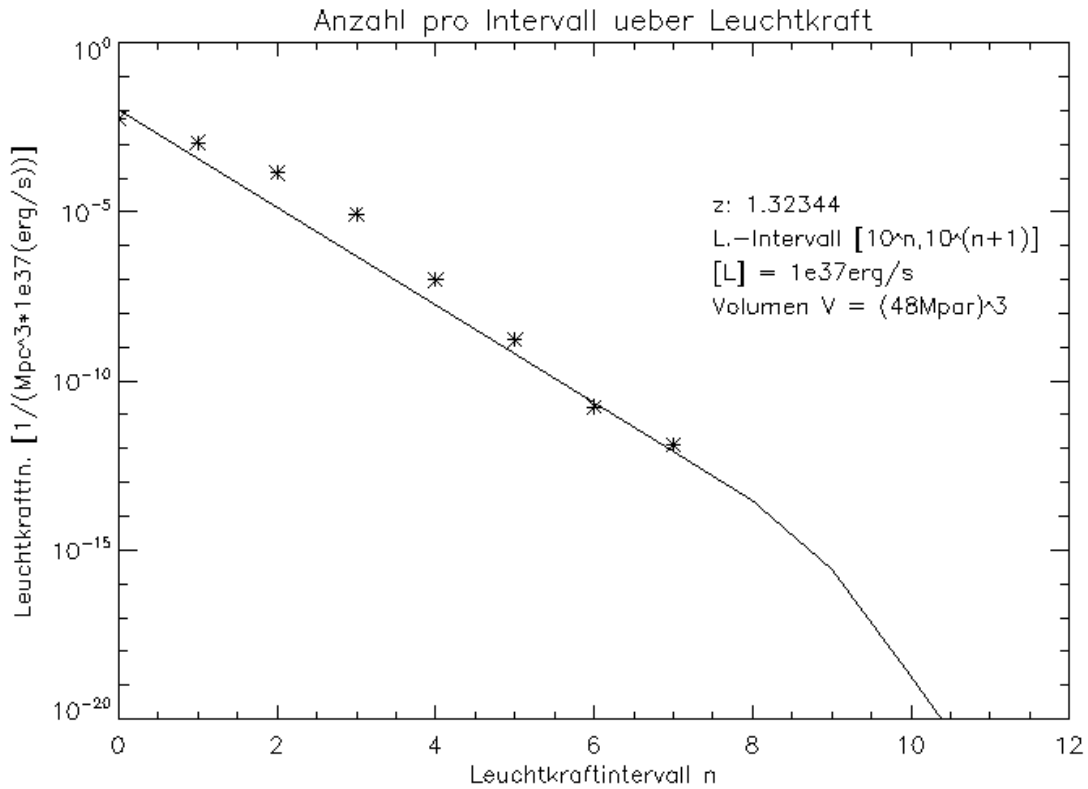
(a) z = 1.323
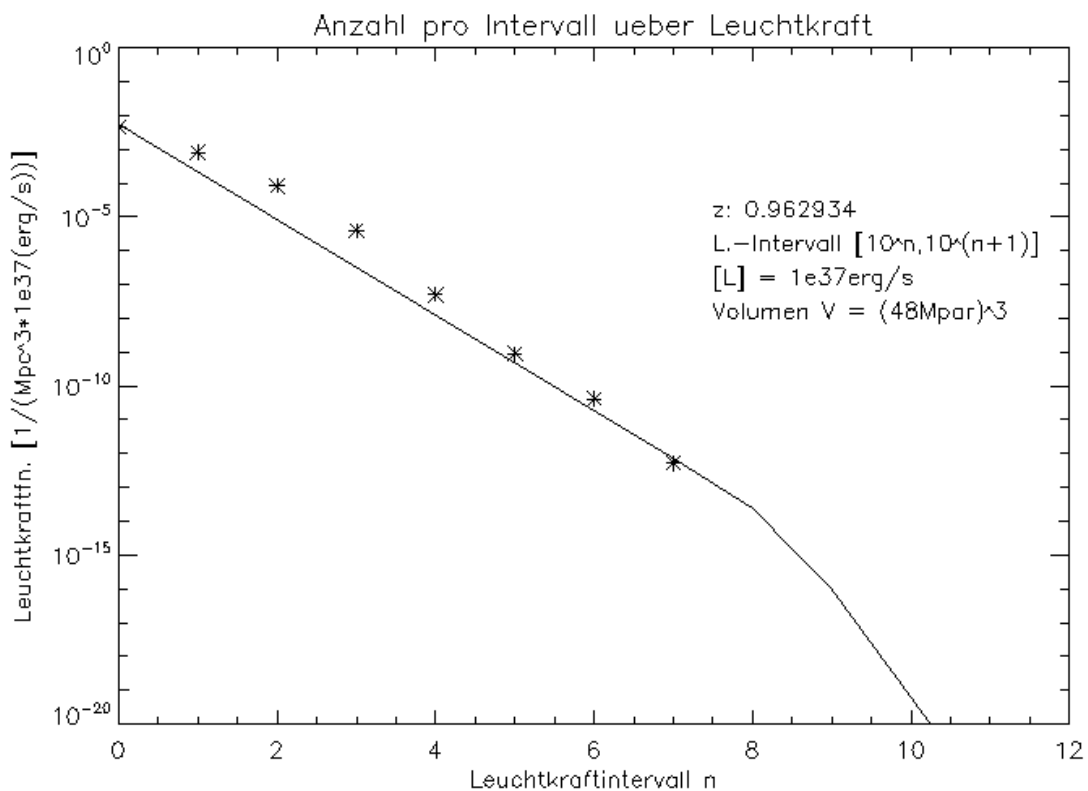
(b) z = 0.963
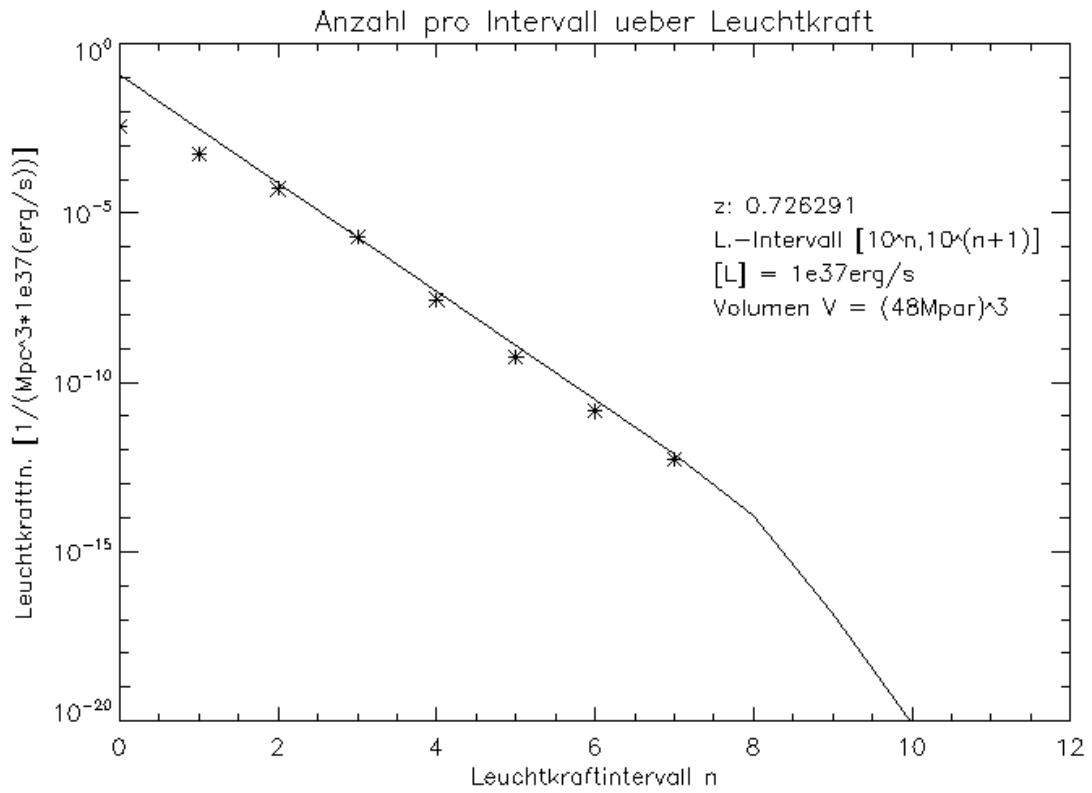
(c) z = 0.726
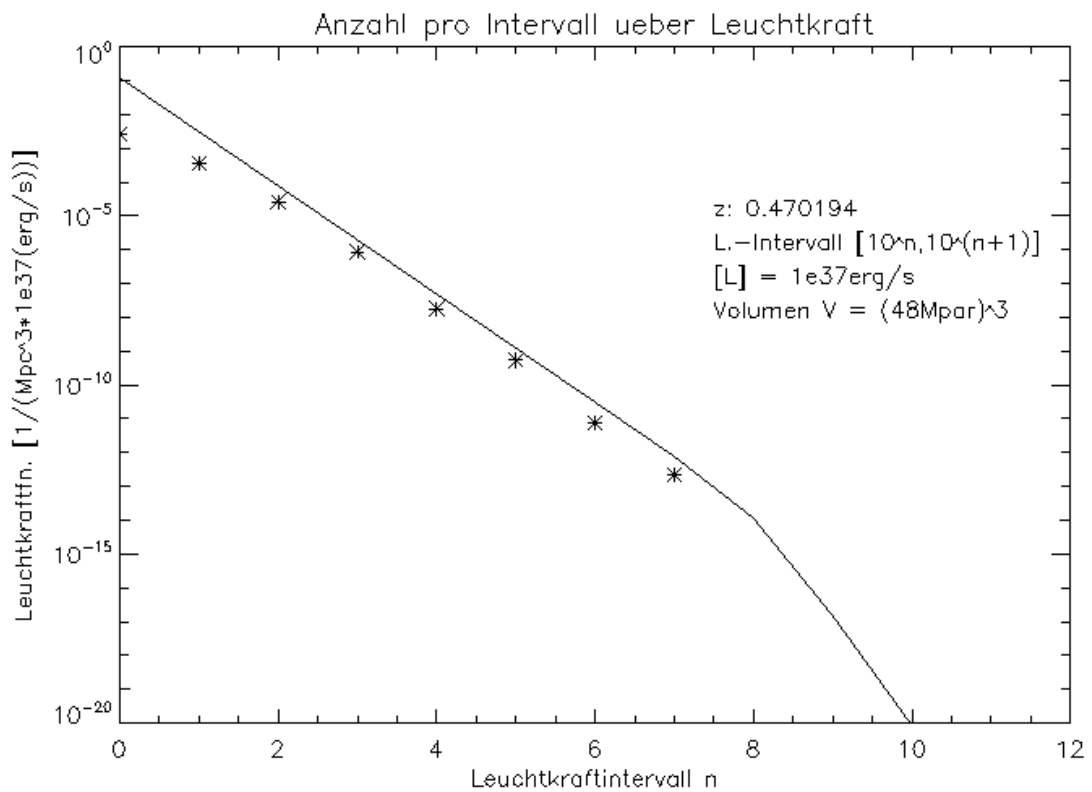
(d) z = 0.470

Summary and conclusion

In Chapter 2 it was said that the growth of mass for black holes in the simulation is primarily determined by accretion. Black holes in the simulation are generated in the centers of galaxies with low masses relative to the mass range of the whole population. Depending on the mass range the black hole is located in, the accretion rates may take high or low values in reference to the Eddington accretion rate. The classification of the mass ranges is different for each resolution, which is shown in tables 2.1, 2.2, and 2.3. In the intermediate mass range, the accretion rate in general is high, which leads to a rapid growth of mass. After crossing the intermediate mass range the accretion rate decreases. This could be due to the fact that most matter in the environment of the black hole in the center of the galaxy was accreted. The minimum in the number per mass range, we see in figures 2.5, 2.6, and 2.7 results of the rapid growth of mass in the intermediate mass range.

It is important to note once again that this behavior is only detectable in the medium and the high resolution simulations for specific redshifts, but not in the ultra high resolution. This difference between mr and hr, on the one hand, and uhr, on the other hand, possibly results of the already mentioned difficulties concerning the simulation of the accretion rate. In the uhr the evolution of black holes starts with lower masses than in the mr and in the hr due to the given mass limit for seeding. As a result, the evolution of the accretion rate in the uhr is not described as good as in the mr and in the hr. This may possibly lead to the not-existence of the intermediate mass range. This is a crucial challenge for the validity of the demonstrated behavior of the black holes.

The comparison of the luminosity function gained by fitting observational data with the calculated luminosity function for the simulated data shows, that the number of AGNs per luminosity interval and volume element in the simulation is in good agreement with observations for particular accretion rate ranges. The consideration of these ranges for the mr and the hr for redshifts lower than z = 0.7 shows, that the occurrence of the minimum in the number per mass range does not influence the

luminosity function for the luminosity ranges corresponding to these accretion rate ranges with high accuracy. For the *mr* this can be seen by the consideration of the accretion rate range, given in Table 2.8, in Figure 2.1, and in the *hr* this can be seen for by the consideration of the accretion rate ranges, given in Table 2.9, in Figure 2.2 for redshifts lower than z = 0.7. This is of specific interest, because, if the minimum would not exist in reality, especially in these accretion rate ranges, where only a few black holes in the intermediate mass occur, the fitted luminosity function would have higher values than the calculated one. One problem for the degree of reliance of this statement is that for the *hr* for redshifts $z > 0.75$ the accretion rate range is to low to issue a statement in this context. Furthermore, the consideration of the data for the *uhr* does not allow statements concerning three different mass ranges. One more problem concerning the occurrence of the minimum is, that the ranges of high accretion rate are not described well in the medium and in the high resolution for redshifts larger than z = 0.7. This can be seen by comparing the accretion rate ranges given in tables 2.8 and 2.9 with the overall accretion rate shown in figures 2.1 and 2.2.

Conclusion. The investigation of the temporal development of black holes in the centers of galaxies, on the one hand, yielded a concept for the evolution of the mass and the accretion rate for growing black holes. On the other hand, evidence were given, that the evolution leads to a minimum in the number per mass range not detectable in the luminosity function. As a result of the problems, especially concerning the *uhr*, further investigation, also including the reliability of the *uhr*, are absolutely necessary to check these conclusions before reliable predictions concerning the number of AGNs per mass range may be given.

Acknowledgment

Appendix

Fundamental physical constants and other measured variables:

- Elementary charge: $e = 1.602 \times 10^{-19} C$

- Gravitational constant: $G = 6.673 \times 10^{-11} m^3 kg^{-1} s^{-1}$

- Speed of light: $299,792,458 ms^{-1}$

- Vacuum permittivity: $\epsilon_0 = 8.854 \times 10^{-12} Fm^{-1}$

- Stefan-Boltzmann law: $\sigma_{SB} = 5.671 \times 10^{-8} Wm^{-2} K^{-4}$

- Thomson cross-section: $\sigma_T = 6.652 \times 10^{-29} m^2$

- Solar mass: $M_\odot = 1.989 \times 10^{30} kg$

- Solar luminosity: $L_\odot = 3.8 \times 10^{33} ergs s^{-1}$

Bibliography

A. Weigert, H.J. Wendker, L. W. (2009). *Astronomie und Astrophysik - Ein Grundkurs*. WILEY-VCH Verlag GmbH and Co. KGaA, Weinheim, fifth edition.

Demtroeder, W. (2005). *Experimentalphysik 1 - Mechanik und Waerme*. Springer Verlag, Berlin, Heidelberg, New York, fourth edition.

Dolag, K., Vazza, F., Brunetti, G., and Tormen, G. (2005). Turbulent gas motions in galaxy cluster simulations: the role of smoothed particle hydrodynamics viscosity. *Monthly Notices of the Royal Astronomical Society*, 364:753–772.

Fabjan, D., Borgani, S., Tornatore, L., Saro, A., Murante, G., and Dolag, K. (2010). Simulating the effect of active galactic nuclei feedback on the metal enrichment of galaxy clusters. *Monthly Notices of the Royal Astronomical Society*, 401:1670–1690.

Fontanot, F., Pasquali, A., De Lucia, G., van den Bosch, F. C., Somerville, R. S., and Kang, X. (2011). The dependence of AGN activity on stellar and halo mass in semi-analytic models. *Monthly Notices of the Royal Astronomical Society*, 413:957–970.

Hopkins, P. F., Richards, G. T., and Hernquist, L. (2007). An Observational Determination of the Bolometric Quasar Luminosity Function. *The Astrophysical Journal*, 654:731–753.

Komatsu, E., Smith, K. M., Dunkley, J., Bennett, C. L., Gold, B., Hinshaw, G., Jarosik, N., Larson, D., Nolta, M. R., Page, L., Spergel, D. N., Halpern, M., Hill, R. S., Kogut, A., Limon, M., Meyer, S. S., Odegard, N., Tucker, G. S., Weiland, J. L., Wollack, E., and Wright, E. L. (2011). Seven-year Wilkinson Microwave Anisotropy Probe (WMAP) Observations: Cosmological Interpretation. *Astrophysical Journal Supplement Series*, 192:18.

Mueller, A. (2010). *Schwarze Loecher - Die dunklen Fallen der Raumzeit.* Spektrum Akademischer Verlag, Heidelberg, first edition.

Schneider, P. (2008). *Einfuehrung in die extragalaktische Astronomie und Kosmologie.* Springer Verlag, Berlin, Heidelberg, New York, second edition.

Shapiro, S. and Teukolsky, S. (1983). *Black Holes, White Dwarfs, and Neutron Stars - The Physics Of Compact Objects.* John Wiley and Sons, Inc, New York, first edition.

Springel, V., Di Matteo, T., and Hernquist, L. (2005). Modelling feedback from stars and black holes in galaxy mergers. *Monthly Notices of the Royal Astronomical Society*, 361:776–794.

Springel, V. and Hernquist, L. (2003). Cosmological smoothed particle hydrodynamics simulations: a hybrid multiphase model for star formation. *Monthly Notices of the Royal Astronomical Society*, 339:289–311.

Springel, V., White, M., and Hernquist, L. (2001). Hydrodynamic Simulations of the Sunyaev-Zeldovich Effect(s). *The Astrophysical Journal*, 549:681–687.

Tornatore, L., Borgani, S., Matteucci, F., Recchi, S., and Tozzi, P. (2004). Simulating the metal enrichment of the intracluster medium. *Monthly Notices of the Royal Astronomical Society*, 349:L19–L24.

Tremaine, S., Gebhardt, K., Bender, R., Bower, G., Dressler, A., Faber, S. M., Filippenko, A. V., Green, R., Grillmair, C., Ho, L. C., Kormendy, J., Lauer, T. R., Magorrian, J., Pinkney, J., and Richstone, D. (2002). The Slope of the Black Hole Mass versus Velocity Dispersion Correlation. *The Astrophysical Journal*, 574:740–753.

Statement of self-reliance

I hereby confirm

that I have written the present thesis independently and without illicit assistance from third parties and using solely the aids mentioned. I am aware that infringement may lead to the deprivation of the academic qualification subsequently.

<u> Munich, September 1st, 2012 </u>

            place, date   signature